https://doi.org/10.5194/essd-2026-99
Preprint. Discussion started: 10 April 2026

Open Access Earth System Science Data Discussions

The ICOS Ecosystem Station Loobos: a pine forest site exposed to atmospheric pollution

Michiel K. van der Molen[1], Henk Snellen[1], Rupert Holzinger[2], Johannes G.M. Barten[1], Hong Zhao[1], Laurens Ganzeveld[1], Julie Fry[1], Wouter Peters[1], Maarten Krol[1], Jordi Vila-Guerau de Arrellano[1], Bart Kruijt[3]

[1]Meteorology and Air Quality group, Wageningen University, Wageningen, the Netherlands

[2]Institute for Marine and Atmospheric Research (IMAU), Utrecht, The Netherlands.

[3]Earth Systems and Global Change group, Wageningen University, Wageningen, the Netherlands

Correspondence to: Michiel K. van der Molen (Michiel.vanderMolen@wur.nl)

Abstract

The Loobos Ecosystem Station (ICOS: NL-Loo) is in a pine forest on sandy soil, the most dominant forest type in the Netherlands. The station was first built in 1995 and the first atmospheric flux measurements were taken in 1997. The station was one of the first in EuroFlux and FLUXNET. Between 2021 and 2023, the station was rebuilt to meet the ICOS standards as an Ecosystem Class 2 station. The initial purpose of the station was to measure fluxes of heat, water and carbon dioxide. Over time, interest has increased in better understanding the forest water use and ecosystem dynamics and its interaction with air quality. This has resulted in additional concentration and flux measurements of ozone and volatile organic compounds. In the near future, we intend to include measurements of nitrogen species (ammonia and nitrogen oxides) to exploit Loobos' unique location downwind of major anthropogenic emission hotspots. Documenting the instrumentation and exploring the quality of the data is important to understand the observational data. This paper therefore describes the station in terms of geography, ecosystem and instrumentation.

1 Introduction

The Loobos station (52.166581 °N, 5.743556 °E, 24 m above mean sea level) is in a pine forest in the Veluwe area, the largest nature area in the Netherlands, where pine is the most dominant species. In 1995, a first tower was built in Loobos to measure water and carbon dioxide fluxes (Dolman et al., 1998, Zhao et al, 2025). As such, it was one of the 17 first FLUXNET stations globally (FLUXNET, 2010), providing a 25-years (1996-2021) observational dataset of meteorology, turbulent fluxes and net ecosystem exchange at the forest (Zhao et al., 2025). In 2018 a grant from the Dutch Science Fund (Ruisdael Observatory, 2026, NWO, 2026) allowed the station to be rebuilt with modern instrumentation in a taller tower according to ICOS instructions. In March 2021 a new robust scaffolding tower was built, which was equipped in subsequent months. In May 2023, the station was officially labelled as one of 40 ICOS (Integrated Carbon Observing System, ICOS Carbon Portal, 2026) ecosystem stations. Documenting measurement stations is important for understanding and interpreting the resulting data. Therefore, this paper describes the geographic history of the site, its ecosystem and the new station's current and planned extension of instrumentation. We focus on long-term continuous and recurring measurements, and briefly mention experimental campaigns. We demonstrate our capability to measure diurnal cycles of CO_2 exchange with eddy covariance and a profile system at the station. This paper describes the instrumentation of the second tower. The first tower's instrumentation is described in Zhao et al. (2025).

https://doi.org/10.5194/essd-2026-99
Preprint. Discussion started: 10 April 2026

Open Access Earth System Science Data Discussions

1.1 Geological history

In Pleistocene times, before the last ice ages (> 238 kyr before present, BP), the Dutch landscape was formed by riverine deposits of sand, gravel and clay, hundreds of meters thick, by the rivers Rhine, Meuse and a few smaller rivers from Germany. In the pre-last ice age, the Saalian, 238-126 kyr BP, the northern part of the Netherlands was covered by ice sheets, which formed glacier tongues towards the South (Berg and Beets, 1987, van der Wateren, 1995, Benneth, 2001). Two glacier tongues formed in the (then) Rhine and Meuse river valley, which are the current IJssel valley and Eem valley. The maximum extension of the glacier tongues occurred around 150 kyr BP. The weight of the ice tongues, which were hundreds of meters thick, pushed up the parent material into push moraines, creating the distinct Veluwe massive topography visible in Fig. Figure 1. The sideway motion caused the originally horizontal layers of riverine deposits to be pushed up diagonally, while smearing clay layers, thus creating (semi)impermeable layers (aquitards) (Bakker and van der Meer, 2023). Boulder loam/glacial till was left behind by the glaciers in the valleys.

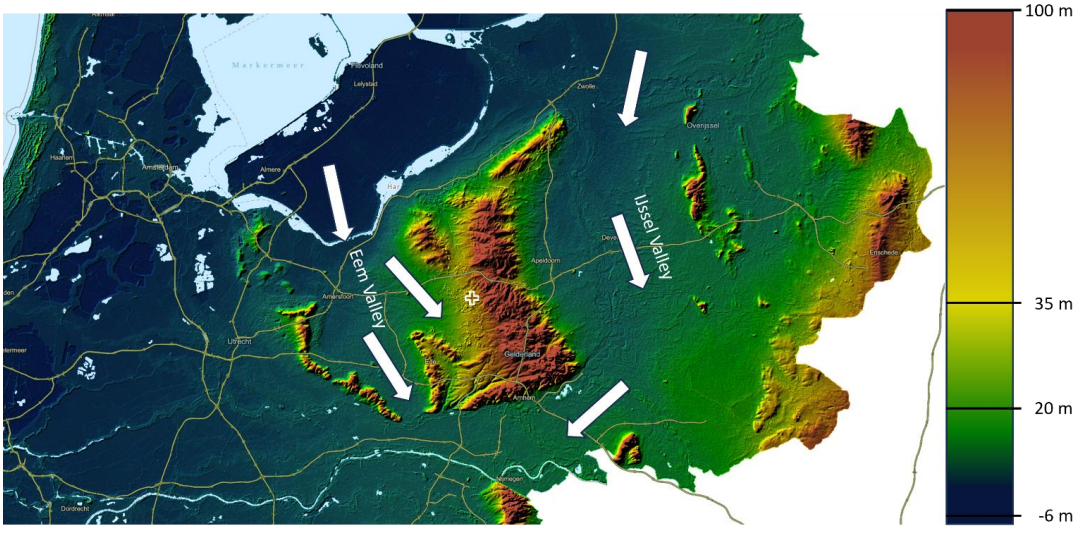

Figure 1. General topography of the center of the Netherlands, with the Veluwe massive in the center as a remnant of the push moraines of the Weichselien ice wedges in the Eem Valley and the IJssel valley. White arrows indicate the direction of the ice wedges. The + mark indicates the location of the station (Source: Esri Nederland, AHN | Powered by ESRI, https://apps.arcgisonline.nl/hoogteviewer/AHN4/DTM/hillshade kleur/@191242.7204296306,457399.1388867902,3 annotated by authors).

In the Saalian and during the transition to the Eemian interglacial period (126-116 kyr BP), the glacier tongues melted, eroding much of the push moraines, while creating meltwater brooks and Sandr plains (Fig. Figure 2). (See also Fig. 2 in Ruegg, 1983).

In the subsequent last ice age (Weichselian, 116 – 11,7 kyr BP), the Scandinavian ice sheets did not reach Netherlands. However, in the governing steppe climate, the landscape developed to a polar desert. The sea level was low and the prevailing Westerly winds deposited 15-30 m of wind-blown fine sand from the dry North Sea basin (Data and Information on the Dutch Subsurface, 2026). The Veluwe push moraine was a barrier, and the majority of the sand was thus deposited in the Eem Valley and on the Western flanks of the Veluwe massive.

In the Holocene, (starting 11,7 kyr BP), the climate became warmer. The loam deposits in the former glacier valleys caused those areas to be poorly drained and peat formation occurred. On the push moraines, the diagonally tilted clay layers still slows down the outflow of ground water towards the sides, causing the main direction of ground water flow to be South to

https://doi.org/10.5194/essd-2026-99
Preprint. Discussion started: 10 April 2026

North, thus preventing fast discharge and maintaining higher ground water tables than without. The push moraines were covered by dense forests.

For long, the Veluwe area remained forested, but starting early in the Middle Ages (ca. 700 AD), the forest was gradually cut for the iron industry and iron- and coppice coal production (Spek and Kleine Koerkamp, 2022), agriculture, and later for wood production for building construction and commercial and military shipping. The poor soil ('Veluwe', in old Dutch 'Vale Ouwe' is Germanic for 'fallow lands') was not very useful for agriculture, so farmers herded sheep to graze on the heather fields and collected the dung in stables where the sheep remained overnight (pot stall system). Overgrazing caused bare soil to be exposed and wind erosion to occur on large scale.

The wind erosion started from the Western flanks of the Veluwe massive (East of the current N310 road shown in Fig. Figure 2). The peat area further West was too wet. On the East side of the N310 road, sand dunes formed (Fig. Figure 2), which increase in height towards the East. At the location of the station, the dunes are 2 to 10 m tall. The sand dunes were most likely deposited on top of former agricultural lands. Some soil cores taken in the soil campaign (section 2.8.3) suggest evidence for this (Section 2.4).

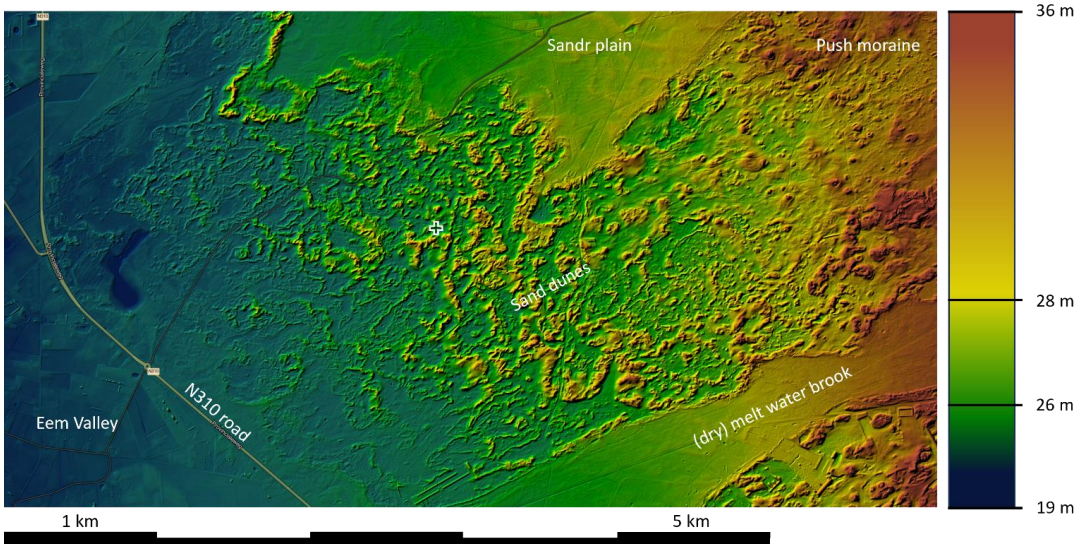

Figure 2. Zoom in on the immediate area around the Loobos station. The increasing height of the sand dunes towards the East of the N310 road is clearly visible. (Source: ESRI Nederland, AHN | Powered by Esri, https://apps.arcgisonline.nl/hoogteviewer/AHN4/DTM/hillshade kleur/@180225.44839508645,463590.4012693153,8 annotated by authors). The plus mark indicates the location of the station.

For centuries, citizens and governments fought the wind erosion and sandstorms, unsuccessfully (Witte, 1916). Finally, starting in 1906, the area was planted with predominantly pine trees, starting along the N310 road and moving towards the East. The patch where the Loobos tower is located was planted in 1911 (Topo Time Travel, Kadaster, 2026).

As a result of the (pre-)historic developments, the area has a wind-blown fine sandy soil. The soil was purely mineral before the trees were planted, hence very poor in nutrients. The trees were planted with a turf of peat, but according to conversations with local people, these trees grew very little until after WOII. On multi-annual timescales, the water table currently varies between 2.5 and 4.5 m below the surface in the valleys between the dunes. It is likely that during the young phase, the water tables were closer to the surface, because large-scale drainage systems were not yet installed to facilitate farming in the Eem Valley. From the 1950's onward, when livestock farming became more intensive, NH_3 emission from the Eem Valley caused deposition in the forest. CLO (2026) provided estimates that the country average deposition rates peaked at 38 kg N ha^{-1} yr^{-1} (24 kg N-NH_y and 14 kg N-NO_x) in the 1990's and decreased afterwards to 21 kg N ha^{-1} yr^{1} (15.4

https://doi.org/10.5194/essd-2026-99
Preprint. Discussion started: 10 April 2026

Open Access Earth System Science Data Discussions

kgN-NH_y and 5.6 kg N-NO_x) in 2023. Regionally, e.g. in the former Eem Valley, deposition rates may be more than double this rate. Melman et al. (2025) estimate the ammonia deposition at 11.6 kg N-NH_3 ha^{-1} yr^{-1} at Speuld in 2010, a nearby experimental site, which is somewhat less exposed to agricultural deposition than Loobos. Melman et al. (2026), using an open-path ammonia sensor in eddy covariance mode at Loobos, measured a NH_3 deposition of 33.3 ± 4.7 kgN ha^{-1} yr^{-1}. Such deposition rates are among the highest in Europe, and signify substantial acidification of the forest soil (de Vries and Du, 2024).

The continuous high nitrogen deposition and input of acidity may cause microbes and fungi to only slowly decompose the deposited pine needles. As a result, a 5-25 cm thick organic layer has formed on top of the mineral soil. In the 2024 soil campaign, we found very few macro-organisms in the soil, no worms. The soil is classified as Podzol according to the international classification of Mantel et al. (2023).

A tree core campaign in 2010, showed that the trees, whose core had been reached, then had 67 to 97 rings (86 on average). Ring widths grew by about 1.25 mm yr^{-1} until the early 1960's. After then, the growth rate was variable between 1 and 3 mm yr^{-1}, with maxima in the mid 1960's, mid 1970's and late 1980's and an average of 2 mm yr^{-1}. From about the year 2000, the area was invaded by Prunus serotina, an exotic broadleaf shrub species. The deposited leaves decompose slowly, because of the absence of endemic species feeding on them.

Despite the accumulation of organic material, the ecosystem respiration seems to decrease over time, while one would expect it to increase with more organic matter present. This could be caused by the increasing acidity over time and associated reduced microbial activity.

This historical and geomorphological perspective explains how the pine forest now grows on originally nutrient poor fine sandy soil which has developed to a Podzol (Fig. Figure 3) under influence of poorly decomposable needles and continuing deposition of reactive nitrogen and associated acidification.

Figure 3. Picture of a Podzol soil pit according to the international classification of Mantel et al. (2023), showing understory vegetation consisting of mosses and vaccinium, a 7 cm thick organic (O) layer, 3 cm thick grey leaching layer (E), a 10-12 cm yellow-red illuviation layer (B), and below the yellow-white parent material (C). Note that the boundary between organic and mineral soil is very sharp, which is a sign of absence of mixing by (micro-)organisms. Picture taken at SP-I-12 on 24 January 2024.

1.2 Ecosystem composition and above ground carbon content

As part of the ICOS labelling procedure (ICOS ETC, 2026), a tree inventory was performed in spring 2023, the results of which provide information about ecosystem composition and provides an estimate of the above ground biomass.

1.2.1 Tree inventory

In two Continuous Plots (CP) with a 25 m radius and 20 Spatial sampling Plots (SP) with a 15 m radius, all trees with a diameter larger than 5 cm at 1.3 m height were identified. Their GPS locations were measured with a sensitive GNSS

https://doi.org/10.5194/essd-2026-99
Preprint. Discussion started: 10 April 2026

receiver (EMLID, Hungary), which, below the canopy, was accurate to within 10 cm. The tree species, diameter and height were identified as well as the health status (Healthy, Minor diseases, Major diseases, Dead, Fallen). All trees were tagged with a unique ID. Tree stumps that fork at or below 1.3 m, were treated as individual trees sharing a common stump. The locations of the CP and SP locations are shown in Fig. Figure 4. The inventory resulted in a database with 1063 trees. The inventory was first done in spring 2023 and according to ICOS instructions will be repeated every 3 years at the CP's and every 10 years at the SP's.

Figure 4. Location of the study area, including the target area (grey square) and the Spatial sampling plots (SP-I). The grey shaded surfaces indicate the location of roads and horse tracks excluded from potential selection for SP locations. The location of the tower is indicated by the 'o' sign marked 'NL-Loo'. The CP's are located in the immediate location of the tower, with CP_01 west of the tower and CP_02 northeast of the tower. The 'target area' is the area of which we aim to understand a.o. the carbon and water fluxes. (© Google Earth, last accessed 4 February 2026)

1.2.2 Species composition

Pinus sylvestris L. is by far the most dominant species sampled, with 651 of all 1063 trees. Table 1 lists the total list of species and their health status (Iserbyt et al., 2026).

Table 1. List of species observed in the 2023 inventory in the CP's and SP's (Fig. Figure 4) and their health status. Here 'Healthy' is defined as no visual indication of damage, where 'damage' is defined by branches that have lost leaves or where leaves have changed colour; The crown is affected by less than 50%. 'Minor diseases' as visual indication of the crown being affected by diseases, herbivory, storm damage. 'Major diseases' as visual indication of the crown being affected by diseases, herbivory, storm damage. Damage is defined branches that have lost leaves or where leaves have changed colour. The crown is affected by more than 50%, but healthy leaves are still present. 'Dead' trees are the ones still standing and 'Fallen' are the ones fallen over. These definitions are according to the ICOS Instruction for ancillary vegetation measurements in forest (2021).

Species	Healthy	Minor diseases	Major diseases	Dead	Fallen	Total
Pinus sylvestris L.	604	11	5	30	1	**651**
Prunus serotina Ehrh.	205	1	3	3	0	**212**
Quercus robur L.	78	0	0	31	0	**109**
Betula pubescens Ehrh.	33	5	1	6	0	**45**
Picea abies (L.) H.Karst.	25	1	2	1	0	**29**
Pinus nigra J.F.Arnold	13	0	0	0	0	**13**
Quercus rubra L.	2	0	0	0	0	**2**

https://doi.org/10.5194/essd-2026-99
Preprint. Discussion started: 10 April 2026

Open Access Earth System Science Data Discussions

Larix decidua Mill.	1	1	0	0	0	**2**
Total	**961**	**19**	**11**	**71**	**1**	**1063**

The Prunus Serotina Ehrh. is an exotic invasive species common in the area. It grows below the Pine canopy often in small shrubs (max 3 m tall), sometimes growing in a tree-like shape up to 7 m tall. The species is not managed and was found to be encroaching the area from about 2000 onwards. Recently, in some parts of the footprint of the tower, the majority of the Prunus shrubs have died, perhaps as a result of extreme drought conditions in 2018 and 2023 and a relatively shallow rooting zone. Another theory is that endemic fungi species such as Taphrina farlowii have started growing on the Prunus serotina (Dutch Mycological Association, 2017). However, this Prunus dying did not largely impact their biomass in the CP's and SP's yet. The Quercus robur L. were all observed in SP-I_15 and SP-I_18, where they are almost the only tree species. It is unknown if these oak trees were planted around the same time as the Pine trees. Apart from these two oak plots, the species composition is comparable between the CP's and SP's (Fig. Figure 5). The average tree density is 478 trees ha^{-1} in the CP's and 568 trees ha^{-1} in the SP's (505 when excluding SP_I-03), so the area weighted average tree density is 499.1 trees ha^{-1} in 2023.

The basal area is 27 m^2 ha^{-1} on average over all plots (Fig. Figure 6). SP-I_05 and SP-I_16 are in a less densely populated part of the forest, which has been potentially subject to thinning. The basal area is dominated by Pine there too. In 2002 an inventory based on 36 randomly selected trees in the same target area resulted in a basal area of 21.4 m^2 ha^{-1}, suggesting an increase of 30% in 21 years.

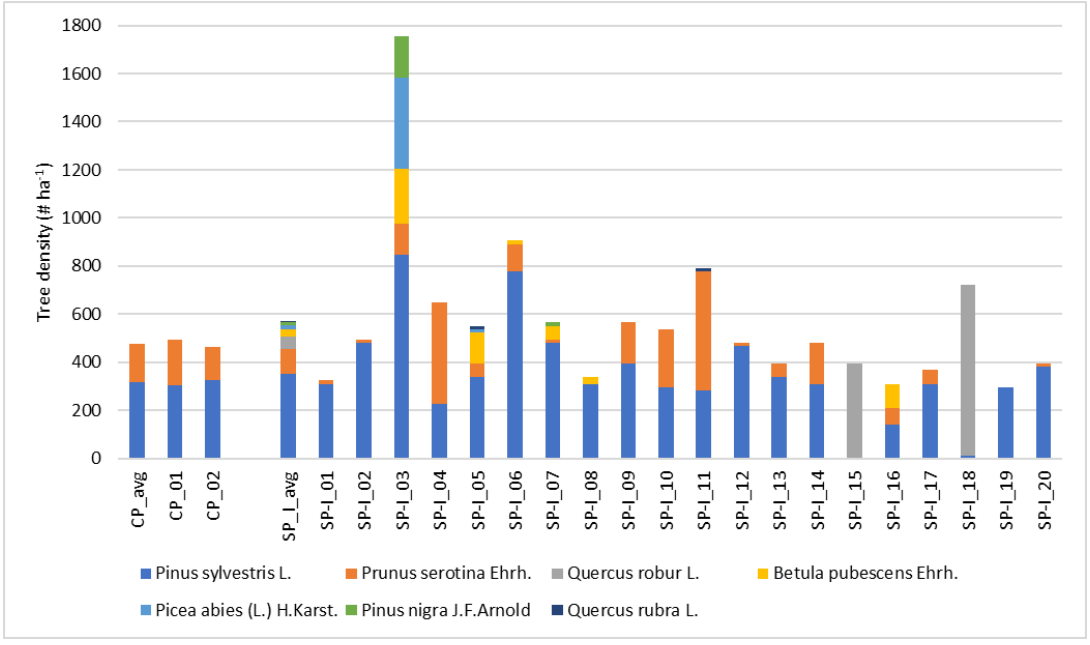

Figure 5. Ecosystem species composition in terms of live tree density (# ha^{-1}) in the CP's and SP's, according to the inventory in spring 2023.

https://doi.org/10.5194/essd-2026-99
Preprint. Discussion started: 10 April 2026

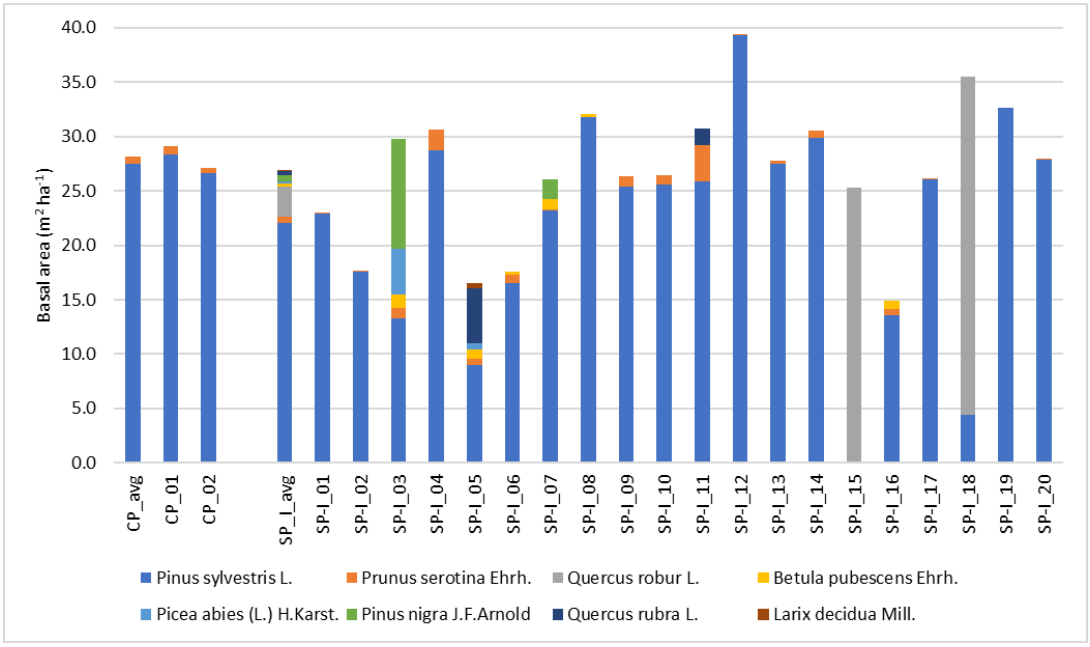

Figure 6. Basal area (m^2 ha^{-1}) of the living trees in the CP's and SP's.

1.2.3 Diameter and height distributions

Figure Figure 7 shows the relative diameter at 1.3 m distribution (Iserbyt et al., 2026). It indicates that the trees dominating the total above ground biomass have a diameter centred around 30 cm (Pinus sylvestris L.) and 20 cm (Quercus rubur L.). The Prunus serotina Ehrh. shrubs and Betula pubescens Ehrh. have diameters centred around 10 cm. The average diameter is 21.3 cm for all trees and 25.0 cm for all non-Prunus serotina trees. Earlier tree inventories in the same target area, but with less samples, show a somewhat larger diameter (Table 5 in Zhao et al., 2025) and an average increase of 0.20 cm per year.

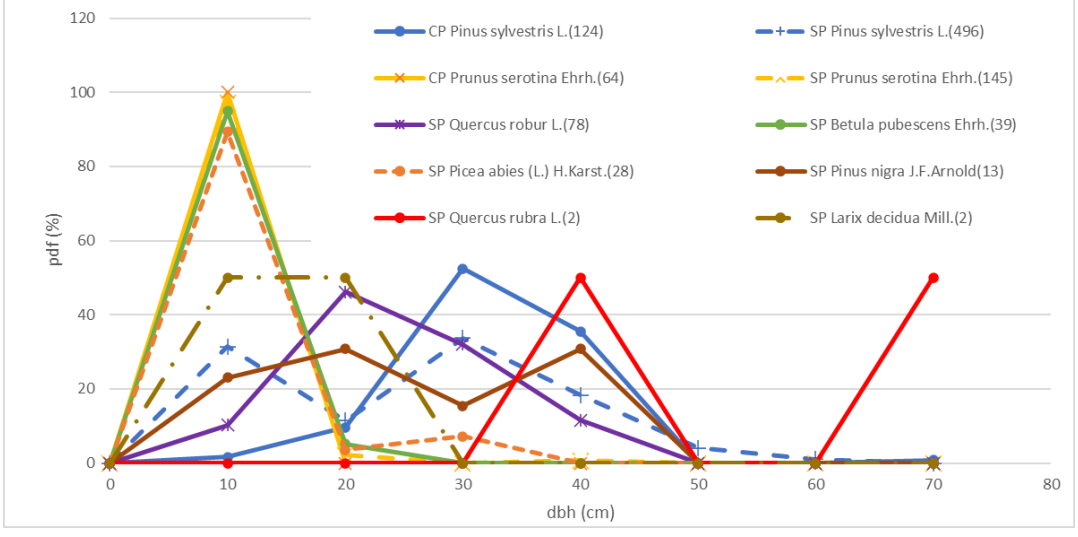

Figure 7. Relative distribution of dbh. The centre of the 10 cm wide diameter classes is shown on the x-axis. The numbers in the legend indicate the number of trees. Dbh (cm) denotes diameter at 1.3 m height, and pdf (%) denotes probability density function.

https://doi.org/10.5194/essd-2026-99
Preprint. Discussion started: 10 April 2026

Open Access Earth System Science Data Discussions

Table 2 shows the average tree height (Iserbyt et al., 2026). It must be noted that the canopy height is more homogeneous than the surface topography, suggesting that the tree height is inversely related to the dune height, i.e. trees on dunes are shorter than trees in valleys between the dunes. Since the tower's base is in a valley and many of the trees around it are on dune slopes and tops, the average canopy height appears to be a height of 20 to 22 m relative to the tower.

Table 2. Average tree height (m) in the CP's and SP's.

Species	CP	SP
Pinus sylvestris L.	18.4 ± 2.0	15.2 ± 4.2
Prunus serotina Ehrh.	6.0 ± 1.7	5.3 ± 2.4
Quercus robur L.		15.2 ± 2.2
Betula pubescens Ehrh.		14.2 ± 4.6
Picea abies (L.) H.Karst.		10.9 ± 3.2
Pinus nigra J.F.Arnold		15.0 ± 3.9
Quercus rubra L.		14.3 ± 0.9
Larix decidua Mill.		11.4 ± 2.7

This tree height matches well with tree height measured in the target area in earlier years (Table 4 in Zhao et al., 2025). These data suggest a growth rate of 16 cm per year. This would extrapolate to an average height of 19.6 m in 2023, which is somewhat taller than the observed height in 2023. However, the diameters reported for these trees are larger too. We hypothesize that the difference is caused by the difference is sample size and geographic distribution of the plots. However, this should be studied in more detail in the near future.

1.2.4 Allometric relations and biomass

To estimate the biomass from the tree diameter, height and species, we used allometric relations. We adopted the relations used in the 7th Dutch Forest Inventory (Schelhaas et al, 2022). The inventory uses Eq.1 to estimate the mass of stem wood and bark:

$$m_{stem+bark} = \frac{\rho_w}{1000} \times d_{tree}^{\alpha} \times h_{tree}^{\beta} \times e^{\gamma} \quad (1)$$

Where $m_{stem+bark}$ refers to the mass of stem wood and bark in kg, ρ_w refers to the wood density, d_{tree} and h_{tree} to the tree diameter at 1.3 m and the tree height. α, β and γ are parameters, the values of which can be found in Table 3. The mass of branches (living and dead), leaves and roots is estimated with Eq. 2:

$$m_X = \kappa \times e^{\lambda + ln(d_{tree}) \times \mu} \quad (2)$$

Where m_X is the mass in kg dry biomass and X refers to the categories 'branches', 'leaves' and 'roots'. κ, λ and μ are species and category dependent parameters (Table 3). Note that the ICOS biomass inventory (Iserbyt et al., 2026) focuses only on aboveground biomass, so we will omit the biomass of roots (although giving the parameters for completeness).

https://doi.org/10.5194/essd-2026-99
Preprint. Discussion started: 10 April 2026

Open Access Earth System Science Data Discussions

Table 3. Parameters to Eqs. 1 and 2 for estimating tree biomass.

Species	ρ_w	Stem wood and bark			branches			leaves			roots		
	kg m^{-3}	α	β	γ	κ	λ	μ	κ	λ	μ	κ	λ	μ
Pinus sylvestris L.	420	1.821	1.074	-2.881	1.045	-3.664	2.160	1.010	-3.528	1.747	0.951	-3.635	2.304
Prunus serotina Ehrh.	400	1.839	0.972	-2.719	1.135	-2.676	2.206	0.956	-4.106	1.321	1.047	-2.618	2.135
Quercus robur L.	580	1.831	1.094	-2.999	1.181	-4.434	2.953	0.966	-4.466	2.138	0.997	-2.863	2.208
Betula pubescens Ehrh.	510	1.592	1.219	-2.791	1.148	-3.819	2.331	1.163	-4.137	1.886	1.044	-1.756	1.876
Picea abies (L.) H.Karst.	400	1.751	1.109	-2.759	1.008	-3.316	2.198	1.020	-2.796	1.869	1.183	-3.739	2.432
Pinus nigra J.F.Arnold	420	1.892	0.954	-2.725	0.999	-1.135	1.468	1.002	-0.611	0.871	0.999	-3.962	2.447
Quercus rubra L.	580	1.839	0.972	-2.719	1.181	-4.434	2.953	0.966	-4.466	2.138	0.997	-2.863	2.208
Larix decidua Mill.	460	1.871	1.006	-2.875	0.967	-3.241	2.141	0.957	-3.885	1.750	1.169	-4.029	2.496

Table 4. Mean ± standard deviation of dry above ground biomass in ton ha^{-1} of live trees estimated using the 2023 tree inventory and allometric relations given above. The means and standard deviations are calculated over 2 CP's and 20 SP's. The dead above ground biomass is not part of the 'Total'. (van der Molen et al., 2026a).

Species	CP's			SP's		
Pinus sylvestris L.	118.8	±	1.7	92.9	±	44.1
Prunus serotina Ehrh.	2.0	±	0.4	1.6	±	2.3
Quercus robur L.	0	±	0	24.8	±	76.5
Betula pubescens Ehrh.	0	±	0	1.1	±	1.9
Picea abies (L.) H.Karst.	0	±	0	0.8	±	3.2
Pinus nigra J.F.Arnold	0	±	0	2.5	±	9.9
Quercus rubra L.	0	±	0	4.2	±	15.8
Larix decidua Mill.	0	±	0	0.1	±	0.4
Total live above ground biomass	**120.8**	**±**	**2.3**	**128.1**	**±**	**51.8**
Dead above ground biomass	9.8	±	2.3	3.6	±	6.5

In a separate plot used in earlier inventories, the above ground biomass was estimated at 121 ton ha^{-1} in 2000, increasing to 151 and 173 ton h^{-1} in 2012 and 2025 (Table 6 in Zhao et al., 2025). Their data suggests a larger biomass, based on fewer trees (N=56-103), than the 2023 inventory (N=1000 trees). Nevertheless, their estimated biomass of comparable, albeit at the larger end of the range of the estimates for the SP's.

The accuracy of those estimates depends on the number of trees measured and the spatial variability, the quality of the measurements, the quality of the allometric relations and the associated parameters. At present, a detailed uncertainty analysis is not available. It is remarkable that the 1996-2025 biomass estimates show a consistent increase, whereas the 2023 estimate (based on more trees in a wider footprint) results in a 35 ton ha^{-1} lower aboveground biomass. The standard deviation of above ground biomass between the SPs is 51.8 ton ha^{-1} and the contribution of standing dead trees is 9.8 ton ha^{-1} in the CPs (3.6 in the SPs). This suggests that spatial variability and dying trees could be responsible for the difference in the 1996-2025 and 2023 ICOS inventories. The accuracy of the allometric relations applied will affect the absolute value of the above ground biomass estimates more than changes in time.

As such, Loobos has a somewhat lower dry above ground biomass than the average in Dutch forests of 177.3 ton dry above ground biomass per ha (Schelhaas et al, 2002, table 13.1). However, it is rather similar to the biomass estimated at the ICOS station in Brasschaat, Belgium (BE-Bra), which has a comparable pine ecosystem and a biomass of 117 ton ha^{-1} in the CP's in 2023 and 102 ton ha^{-1} in the SP's in 2020, based on the ICOS conform tree inventory at that station.

https://doi.org/10.5194/essd-2026-99
Preprint. Discussion started: 10 April 2026

2 Instrumentation

In this section we describe the tower and its instrumentation in separate sections for 1) infrastructure, 2) radiation measurements, 3) soil measurements, 4) meteorological measurements, 5) ICOS eddy covariance measurements, 6) vertical profile measurements, 7) additional concentration and flux measurements of VOC's and ozone, 8) intermittent ecosystem measurements and 9) occasional campaigns. We summarise the instruments and the variables per section in a table. The table contains the instrument type, manufacturer and model, the serial number (SN), the instrument height, eastward and northward distance with respect to the centre of the tower's base and the names of the variables measured.

The variable names have subscripts H, V and R, where H refers to the horizontal index number, V to the vertical index number and R to the replacement index number. For example, in a single vertical soil profile, each instrument has the same H index and consecutive V indices. If an instrument is replaced by another instrument, the R index is increased by one. A second soil profile has a higher H index and can have the same V-indices.

2.1 Infrastructure: Tower, power and internet connection

The tower is built of scaffolding material (Layher) with a surface spanning 2.57 m × 2.57 m. Stairways lead one up the tower. The highest platform is at 36 m (Fig.). In that picture, the left corner points towards the North and the right one to the South. The station coordinates in the WGS 84 system are: Latitude 52.166581 °N and Longitude 5.743556 °E. The UTC offset is equal to +01h and the elevation is 24 m above sea level. The site is marked by the following climate characteristics: mean annual (above canopy) temperature 10.2 °C, mean annual precipitation 900 mm and mean annual global incoming radiation 114 W m^{-2}, positioning it in the temperate oceanic climate (Cfb) Köppen-Geiger climate classification (Geiger, 1954). Next to the tower (Fig. Figure 8) a shipping container is placed, where electricity is available (3x25A, 19kW). A local area network is present, with a 4G connection to the internet.

Figure 8. The Loobos tower, picture taken towards the East (31 March 2025).

https://doi.org/10.5194/essd-2026-99
Preprint. Discussion started: 10 April 2026

2.2 Radiation measurements and PhenoCam

Four component (shortwave and longwave, incoming and reflected/outgoing) radiation measurements are made with a CNR4 radiometer (Kipp & Zn, Table 5). The instrument is mounted on a 3.52 m long pole pointing towards the southwest from the southern point of the tower at a height of 37 m, 15 m above the canopy top. The instrument is equipped with a level (roll and pitch), which are logged with the data and used to level the instrument after cleaning. A backup global radiometer (CM21, Kipp & Zn) was installed at the top of the tower at 38.2 m.

Incoming and reflected photosynthetically active radiation are measured with two SKP215 PAR Quantum sensors, mounted on the same pole as the CNR-4 (Table 5). The PAR sensors are sensitive to radiation of wavelengths between 400 and 700 nm.

The CNR4 and PAR instruments measuring incoming radiation do not suffer from shadows cast by the tower or other structures. The backup global radiometer is exposed to a daily shadow from the lightning deflector. The instruments measuring reflected/outgoing radiation have the tower in about 10% of its field of view. All radiometer data are sampled and stored at an interval of 2 s. These data are available via van der Molen et al. (2026b, 2026c, 2026f, 2026g).

Table 5. Specification of radiometers. *: SW_IN_2_1_1 is part of the backup meteorology system (Section Error! Reference source not found.**)**

MODEL	SN	HEIGHT (m)	EASTWARD DISTANCE (m)	NORTHWARD DISTANCE (m)	VARIABLE_H_V_R
Four components net radiometer Kipp & Zn CNR4	131328	37	3.01	-4.83	SW_IN_1_1_1
					SW_OUT_1_1_1
					LW_IN_1_1_1
					LW_OUT_1_1_1
Pyranometer Kipp & Zn CM21	940188	38.2	1.285	-1.285	SW_IN_2_1_1*
Incoming Photosynthetically Active Radiation Skye SKP215	52771	37	2.7	-4.5	PPFD_IN_1_1_1
Reflected Photosynthetically Active Radiation Skye SKP215	52772	37	2.7	-4.5	PPFD_OUT_1_1_1

A StarDot Netcam SC5 IR was installed at 35 m height in the tower facing the North. Images are collected hourly from 10:30 to 17:30h CET. Images are automatically uploaded to 'PhenoCam, an Ecosystem Phenology Camera Network' operated by the Northern Arizona University (Richardson et al, 2018) and automatically analysed for green chromatic coordinate (GCC) and normalised difference vegetation index (NDVI). All images and results can be viewed via PhenoCam (2026) (Richardson et al., 2018, Seyednasrollah et al., 2019). The GCC and NDVI time series show similarity with the LAI measurements (Zhao et al, 2025), i.e. a peak in August and low values between November and April.

2.3 Continuous soil measurements

Continuous soil measurements are taken at 4 plots around the tower (Fig. S.1). At each plot, the soil heat flux (G) is measured along with soil temperature (TS) at 1.5 and 5.0 cm deep (Campbell CS107), as well as soil water content (SWC). Only at the West and North locations, water table depth (WTD) and a deeper profile of SWC and TS are measured, at depths of 5, 10, 20, 50 and 100 cm. Table 6 provides a complete overview over which variables are measured at which plot with what instrument model. The West plot is on the SE facing flank of a dune, the North plot is on top of a 2 m high dune

https://doi.org/10.5194/essd-2026-99
Preprint. Discussion started: 10 April 2026

underneath the first tower, within centimetres from the soil sensors associated with the first tower, to continue the first tower's time series. The East and South plots are in a valley between the dunes.

The soil heat flux plates (Hukseflux HFP01SC) are self-calibrating. One of the plates self-calibrates every third hour in a N-E-S-W rotation starting at midnight. During the self-calibration, the flag variable G_ISCAL is set to 1. The latest sensitivity factor is stored in the variable G_SF.

The WTD sensor measures the pressure of the soil water column above it and hence the reading depends on the installation depth. The West WTD sensor's head is 8.88 m below the tower's base and the North sensor's head 9.59 m. Hence it follows that WTD_1_1_1 (m) is related to WCP_1_1_1 (Pa) as:

$$WTD\_1\_1\_1 = -8.88 \frac{WCP\_1\_1\_1}{g \times \rho_w}$$

and WTD_2_1_1 (m) is related to WCP_2_1_1 (Pa) as:

$$WTD\_2\_2\_2 = -9.59 + \frac{WCP\_2\_1\_1}{g \times \rho_w}$$

with ρ_w = 998.2 kg m^{-3} at 20 °C and g = 9.81 m s^{-2}. All soil variables are logged by a single Campbell CR1000X datalogger at a sample interval of 1 minute. These data are available via van der Molen et al. (2026b, 2026c, 2026f, 2026g).

Table 6. Continuous soil measurements. G: Soil heat flux (W m^{-2}), G_ISCAL: Flag for measurements during self-calibration (1=yes, 0=no), G_SF: Sensitivity Factor (V / (W m^{-2})), TS: Soil Temperature (°C), SWC: Soil Water Content (m^3 m^{-3}), WCP: Water Column Pressure (Pa), WTD: Water Table Depth (m), T_WTD: Soil Temperature from WTD sensor. The header row indicates the location of the plots relative to the centre of the tower. The variables marked with (*) are logged as raw voltages too.

Instrument; Variable	depth (cm)	West (CP_01) 11 m S, 32 m W	North (CP_02) 9 m N, 9 m E	East 2 m S, 41 m E	South 29 m S, 17 m E
Hukseflux HFP01SC; G (*), G_ISCAL, G_SF	5.0	G_1_1_1 G_ISCAL_1_1_1 G_SF_1_1_1	G_2_1_1 G_ISCAL_2_1_1 G_SF_2_1_1	G_3_1_1 G_ISCAL_3_1_1 G_SF_3_1_1	G_4_1_1 G_ISCAL_4_1_1 G_SF_4_1_1
Campbell CS107; TS	1.5	TS_1_1_1	TS_2_1_1	TS_3_1_1	TS_4_1_1
	5.0	TS_1_2_1	TS_2_2_1	TS_3_2_1	TS_4_2_1
Campbell CS655; SWC (*), TS	5.0	SWC_1_1_1 TS_1_2_2	SWC_2_1_1 TS_2_2_2	SWC_3_1_1 TS_3_2_2	SWC_4_1_1 TS_4_2_2
	10.0	SWC_1_2_1 TS_1_3_1	SWC_2_2_1 TS_2_3_1		
	20.0	SWC_1_3_1 TS_1_4_1	SWC_2_3_1 TS_2_4_1		
	50.0	SWC_1_4_1 TS_1_5_1	SWC_2_4_1 TS_2_5_1		
	100.0	SWC_1_5_1 TS_1_6_1	SWC_2_5_1 TS_2_6_1		
Campbell CS451; WCP, WTD, T_WTD		WCP_1_1_1 WTD_1_1_1 T_WTD_1_7_1	WCP_2_1_1 WTD_2_1_1 T_WTD_2_7_1		

2.4 Precipitation, air pressure, temperature, humidity and backup system

Precipitation (P_1_1_1) is measured with a MPS TRwS 4E15 weighing rain gauge. The rain gauge is installed in a separate tower 57.7 m North and 25.7 m East of the tower's base at a height of 15.3 m. As such it is located in a small opening in the forest where the surrounding trees function as a wind shield. The horizontal distance to the tree tops is 2 to 4 times the height difference (i.e. the angles are between 14 and 26.5 °).

https://doi.org/10.5194/essd-2026-99
Preprint. Discussion started: 10 April 2026

Air pressure is measured with a Bosch BMP390 at a height of 35 m in the tower. The height difference between the sensor and the tower base is not corrected for, nor is the pressure converted to sea level pressure.

Air temperature (TA_1_1_1) and relative humidity (RH_1_1_1) are measured at the top of the tower at 38.2 m with a mechanically ventilated and sun shielded Vaisala HMP155 (Section 2.6). The sample collection and storage interval are both 20 s.

A backup meteorological system is installed, intended to measure a few variables, key for applying the ICOS gapfilling procedure (ONEFLUX, Pastorello et al., 2020), in case a power or system failure occurs. The backup system operates entirely independently from the other systems and is powered by a battery. It consists of a Campbell CR1000X datalogger, powered by a battery, which is charged from a separate group in the electrical distribution box. The datalogger logs the signals of the Kipp & Zn CM21 Pyranometer (SW_IN_2_1_1, 38.2 m, section 2.2), a second Vaisala HMP155 sensor (TA_3_1_1 and RH_2_1_1, 38.2 m, section 2.6) and a Young 52203 rain gauge (P_2_1_1, 37.7 m). Each of these instruments is installed at the top of the tower. The backup rain gauge is not shielded, which causes the observed precipitation to be underestimated by about 10% relative to the precipitation observed by the weighing rain gauge, shielded by the tree tops (P_1_1_1). The sample collection and storage interval are 20 s. These data are available via van der Molen et al. (2026b, 2026c, 2026f, 2026g).

2.5 ICOS compliant eddy covariance measurements

Turbulent flux measurements are caried out with the eddy covariance technique using a Gill HS-50 ultrasonic anemometer and a Li-COR LI7200RS enclosed CO_2 and H_2O gas analyser mounted on top of the tower at 38.2 m, ~16 m above the forest canopy. The horizontal head of the anemometer is directed towards the prevailing wind direction (SW), 1.75 m outside the tower structure. The gas analyser is mounted downwind from the anemometer and draws in air from just outside the anemometer's sample volume via a 0.71m long 6 W heated tube with an inner diameter of 5.33 mm and a flow rate of 10 L min^{-1}. The anemometer measured three components of wind velocity and sonic temperature at 50 Hz. The gas analyser measures CO_2 and H_2O concentration at 20 Hz. Signals from both instruments are collected by a Li-COR Smartflux2 system, which co-locates both data streams with GPS time to an output with frequency 20 Hz (Fratini et al, 2018). More specifications are provided in Table 7.

https://doi.org/10.5194/essd-2026-99
Preprint. Discussion started: 10 April 2026

Open Access Earth System Science Data Discussions

Table 7. Technical specifications of the eddy covariance system.

MODEL	GA_CP-LI-COR LI-7200RS	SA-Gill HS-50
SN	72H-0920	H184704
HEIGHT (m)	38.2	38.2
EASTWARD DISTANCE (m)	-4.15	-4.15
NORTHWARD DISTANCE (m)	0.35	0.35
SAMPLE OUPUT INTERVAL (s)	0.05	0.05
LOGGER	1 (Smartflux)	
FILE NUMBER	2 2	
FLOW_RATE (L min^{-1})	10	-
Flow Module SN	FM1-0678	-
Smartflux SN	AIU-2066	-
Sonic Anemometer North offset (degrees)	-	270
Sonic Anemometer Wind format	-	U, V, W
Sonic Anemometer Align	-	Spar
Sensor separation (vertical, m)	-0.03	
Sensor separation (Eastward, m)	0.11	
Sensor separation (Northward, m)	0	
Wind direction exclusion (direction, degrees)	90	
Wind direction exclusion (range, degrees)	20	
Variable names (*) **(*) These variable names do not follow the H_V_R notation.**	U, V, W, T_SONIC, SA_DIAG_TYPE, SA_DIAG_VALUE	CO2_CONC, H2O_CONC, CO2_POW_SAM, H2O_POW_SAM, CO2_POW_REF, H2O_POW_REF, CO2, H2O, CO2_DRY, H2O_DRY, T_CELL, T_CELL_IN, T_CELL_OUT, PRESS_CELL, PRESS_DELTA, FLOW_PRESS, FLOW_VOLRATE, GA_DIAG_CODE, GA_TUBE_HEAT, GA_TUBE_HEAT_V, GA_CHKSUM

The 20Hz data are collected in zipped 30-minute CSV files. These files are sent to the ICOS Carbon Portal for further processing of the raw data into fluxes, quality assurance and gap filling. The raw as well as the processed data can be retrieved from the ICOS Carbon Portal (2026) and in van der Molen et al. (2026d, h).

Figure Figure 9 shows the climatological footprint of the eddy covariance fluxes around the tower, where the 50, 70, 80 and 90% cumulative footprint isopleths (Kljun et al., 2015) are show with respect to the target area in unstable ((z-d)/L< -0.2 and stable ((z-d)/L > 0.2) conditions. The typical radius of the 80% isopleth is 270 m in unstable conditions and 500 m in stable conditions. Even the 90% footprint is almost entirely within the target area. The flux data are available via van der Molen et al. (2026d, 2026e, 2026f, 2026i).

https://doi.org/10.5194/essd-2026-99
Preprint. Discussion started: 10 April 2026

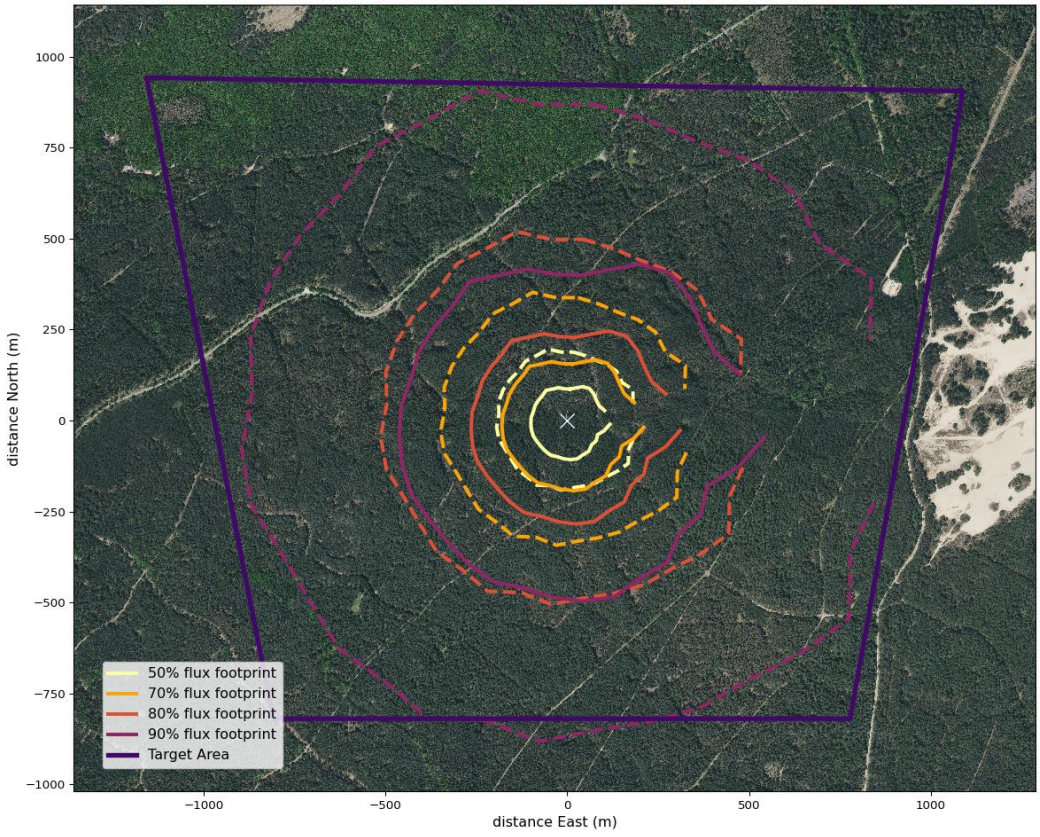

Figure 9. Footprint climatology of the turbulent fluxes measured at the EC tower in relation to the extent of the target area. The 50, 70, 80 and 90% cumulative contribution isopleths are shown. The solid lines represent the footprint area in unstable conditions ((z-d)/L < -0.2) and the dashed lines in stable conditions ((z-d)/L > 0.2). The white crossmark in the center indicates the location of the tower. The isopleths are interrupted towards the east, because this area is excluded from flux calculations, as the tower blocks the wind from those areas. (Background aerial photograph 8 cm RGB, pdok.nl, 2026).

2.6 Below-canopy profile of CO_2 and H_2O concentrations, temperature, wind speed and direction and leaf wetness

The eddy covariance system is installed at a height of 38.2 m, while the tree canopy is densest roughly between 16 and 22 m. Hence in stable atmospheric conditions, turbulence may not be strong enough to mix air from the ground and canopy space to the height of the eddy covariance system. Hence emissions (or deposition) of gases, moisture and heat, may lead to the accumulation (or depletion) of concentrations and heat in the below-canopy space and remain (partially) undetected as turbulent fluxes by the eddy covariance system. After transitioning to an unstable atmosphere, the gases, moisture and heat will be mixed to the level of the eddy covariance system again and cause a delayed response. Assuming no net horizontal advection, the sum of accumulation in stable conditions and release in unstable conditions over a day is supposedly zero over 24 hours (strictly speaking between well mixed moments, e.g., afternoons of consecutive days).

To quantify the below-canopy storage of CO_2, water vapour and heat, these variables are measured along a vertical profile along the tower. CO_2 and H_2O mixing ratios are measured at 11 levels, temperature and wind speed at 5 levels (Table 8). The number of 11 levels is chosen such that interpolation errors do not account for more than 5% of the relative flux. The distribution of levels follows a logarithmic profile, which is slightly adapted to the levels of the platform in the tower to

https://doi.org/10.5194/essd-2026-99
Preprint. Discussion started: 10 April 2026

access the instruments. From the change in concentrations and temperature in time and the thickness of the representative air space, the accumulated CO_2, water vapour and heat are calculated as:

$$F_X = \frac{1}{dt} \int_{z=0}^{h_{EC}} X \, dz \quad (3)$$

where *F* represents the so-called storage flux, dt the integration time (30 minutes in this study), z the height along the tower, h_{EC} the height of the eddy covariance system (38.2 m), and X the variable (i.e., CO_2, H_2O or temperature).

Analysis of measurements along a profile in the first tower (Zhao et al, 2025) shows that storage fluxes of CO_2 may be in the order of -5 and +3 µmol m^{-2} s^{-1}, hence making up a relatively large part of the total fluxes. For water vapour and heat, the contribution of the storage fluxes is considerably smaller. Hence the resolution of the CO_2 (and H_2O) profile is finer than for temperature.

A single Li-COR LI-850 gas analyser is employed to sequentially measure the concentrations at each of the 11 levels (Fig. Figure 10. Schematic of the profile system's design at Loobos.). The inlets are protected with precipitation shields. At the inlets, an air suction filter (ZFC 050-04B, SMC, Japan) is installed to filter out particulate matter (5 µm, 95% filtration efficiency) and to reduce pressure to about 80kPa to prevent condensation in the tubing. The air is then drawn to a 3.5 L buffer volume (DURAN™ GLS 80™) to dampen short-term variations in concentrations. Behind the buffer volumes, the tubes are connected to 3-way pneumatic solenoid valves (EVT317V-6DZ-02). One end of each outlet is connected to a mass flow regulator (EL-FLOW Base F-201CB, Bronkhorst, the Netherlands), which maintains a constant flow rate of 1 L min^{-1} in each line. The other end of each outlet is connected to the gas analyser, behind which is the same type of mass flow regulator, maintaining 1 L min^{-1} through the gas analyser as well. All tubes are Teflon (PTFE) with an inner diameter of 4 mm. The use of Teflon was preferred over PUR (Polyurethane) tubes (SMC TU0604B-20), which appeared to incur condensation more than Teflon tubes. All fittings are one-touch fittings (SMC Metric Size KQ2). A 200 L min^{-1} vacuum pump (Pfeiffer Vacuum HiScroll 12 ATEX) draws the air through each of the lines.

https://doi.org/10.5194/essd-2026-99
Preprint. Discussion started: 10 April 2026

Table 8. Below-canopy profile measurements of CO_2 and H_2O concentrations, temperature (T), wind speed (WS) and wind direction (WD), relative humidity (RH) and their heights. The third row indicates the instrument model, the fourth row the sample collection frequency and the subsequent rows indicate the variable names. In the case of CO_2 and H_2O, the variable name is the same for all levels, where a separate variable (LEVEL) indicates the level number. *; TA_3_1_1 and RH_2_1_1 are part of the backup meteorology system (Section 2.4).

Height	number of inlets	CO_2	H_2O	T	WS, WD	T, RH	Leaf wetness
m	-	mmol m^{-3}	mmol m^{-3}	°C	m s^{-1}, degrees	°C	mV
		Li-COR LI-850	Li-COR LI-850	Generic PT-100	Gill WindSonic4	Vaisala HMP155	Meter Pythos31
Sample interval (s)		1 s	1 s	20 s	20 s	20 s	60 s
38.2	1	CO_2 (level 1)	H_2O (level 1)	TA_2_1_1	WS_2_1_1 WD_2_1_1	TA_1_1_1, RH_1_1_1 TA_3_1_1* RH_2_1_1*	
30.0	1	CO_2 (level 2)	H_2O (level 2)				
22.1	1	CO_2 (level 3)	H_2O (level 3)	TA_2_2_1	WS_2_2_1 WD_2_2_1		LWmV8
20.0							LWmV7
18.0							LWmV6
15.7	1	CO_2 (level 4)	H_2O (level 4)	TA_2_3_1	WS_2_3_1 WD_2_3_1		LWmV5
11.2	1	CO_2 (level 5)	H_2O (level 5)				LWmV4
7.4	1	CO_2 (level 6)	H_2O (level 6)	TA_2_4_1	WS_2_4_1 WD_2_4_1		LWmV3
4.5	1	CO_2 (level 7)	H_2O (level 7)				LWmV2
2.4	1	CO_2 (level 8)	H_2O (level 8)	TA_2_5_1	WS_2_5_1 WD_2_5_1		LWmV1
1.5	2	CO_2 (level 9)	H_2O (level 9)				
0.4	2	CO_2 (level 10)	H_2O (level 10)				
0.1	4	CO_2 (level 11)	H_2O (level 11)				
-	1	CO_2 (level 12, high)	H_2O (level 12, zero)				
-	1	CO_2 (level 13, low)	H_2O (level 13, zero)				

The levels 12 and 13 are connected to gas cylinders with known gas concentrations (464.64 ppm and 367.93 ppm CO_2, zero H_2O). The two lowermost are ramified with two inlets at 1.5 and 0.4 m and 4 inlets at 0.1 m. The levels below 5 m are installed in a separate mast next to the main tower, as the tower is fenced off with solid multiplex boards (Fig. Figure 8). The tubing is led underground to the buffer volumes. The underground parts are heated about 1 °C above the soil temperature to prevent condensation in the tubes.

A Campbell Scientific CR1000X datalogger logs the gas analyser's digital 1 Hz output. Besides CO_2 and H_2O concentrations, the volume flow rate (FLOW_VOLRATE), cell temperature and pressure (T_CELL, PRESS_CELL) are sampled. The datalogger also controls the switches via a Raspberry Pi embedded controller. The switches are set every 30 s to sample each of the lines 1 to 11 sequentially. The two calibration gasses (levels 12 and 13) are sampled at midnight (0h) and noon (12h) each day for 30 s each. As a result, all levels are sampled with a return time of 5.5 min (6.5 min including calibration levels). A linear least squares regression is used to calibrate the CO_2 concentration measurements for the next 12h. The calibration coefficients are stored. The slopes are typically between 0.95 and 1.05 over a longer period (2 years) and vary with an amplitude less than 0.02 over a month. The instrument's water vapour response is calibrated a few times per year with a Li-COR LI-610 dew point generator. The temperature profile is measured using mechanically ventilated generic PT-100 Class 1/3 DIN thermometers at the 5 levels (Table 8). Gill Windsonic4 at the same 5 levels measure wind

https://doi.org/10.5194/essd-2026-99
Preprint. Discussion started: 10 April 2026

speed and wind direction. The profile system is complemented with air temperature and relative humidity measurements with two Vaisala HMP155 sensors, one 'regular' (TA_1_1_1 and RH_1_1_1) and one backup (TA_3_1_1 and RH_2_1_1, Section 2.4) at the top of the tower. The data are available via van der Molen et al. (2026a, 2026b, 2026c, 2026d, 2026f, 2026g, 2026h).

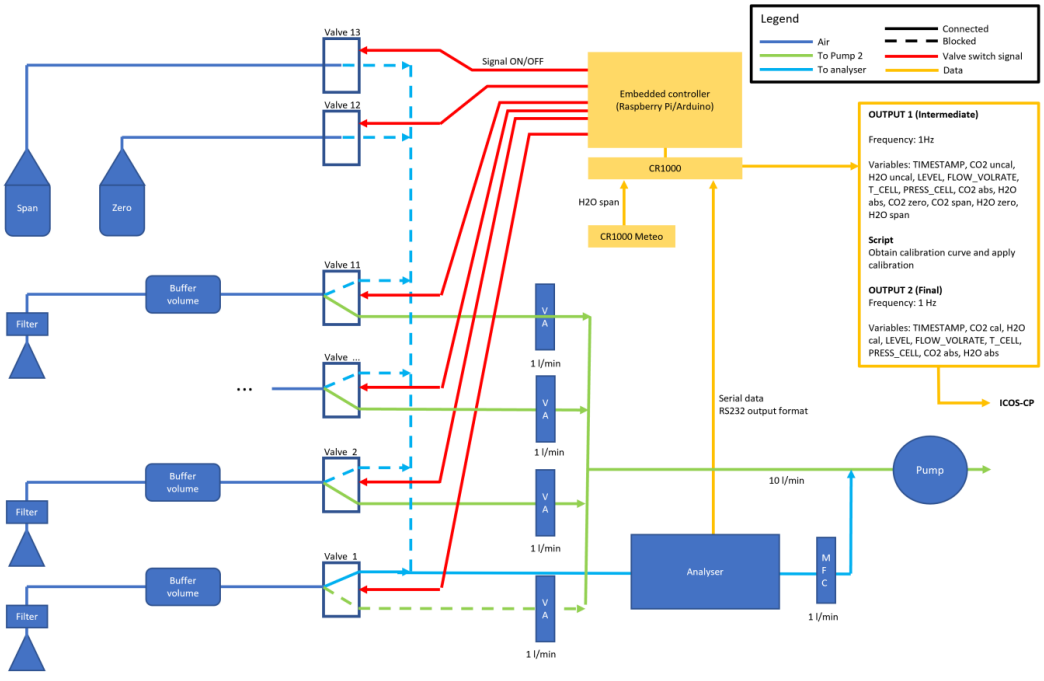

Figure 10. Schematic of the profile system's design at Loobos.

A profile of 8 leaf wetness sensors (Meter Environment Pythos31) was installed along the tower in August 2023 (Table 8), from the canopy top downward. The sensors measure the electrical conductance on an artificial leaf surface, which increases with the wetness of the leaves. The sample interval is 1 minute. Being non-ICOS standard, these data are only accessible at MAQ Observations (2026) and especially relevant for analysis of the role of canopy wetness in the exchange of reactive compounds such as nitrogen compounds, ozone and BVOCs.

2.7 Additional eddy covariance measurements of VOC and ozone

Volatile Organic Compound (VOC) and Ozone (O_3) concentrations and fluxes are measured at the station since the year 2022 and 2025, respectively. These species interact with the ecosystem's canopy conductance, carbon uptake and transpiration. Regional emissions of reactive oxidized nitrogen, NO_x, reactive reduced nitrogen, NH_y, and VOCs affect the ozone and reactive nitrogen species chemistry, concentrations and deposition, which influence nutrient availability for plant growth and acidity. We first describe the methods to measure concentrations and then briefly outline the methods of flux calculations.

2.7.1 Concentration measurements

VOC concentrations are measured with a Proton-transfer-reaction mass-spectrometer (PTR-MS). The instrument was installed in November 2022. Ambient air is sampled through a 56 m long ~50 m PFA tubing (ID=6 mm) from close by the sonic anemometer at 38.2 m above the ground (Section 2.5) to the instrument which is placed in the sea container (Section 2.1). Between the tower and the sea container the line is led trough a PVC tubing buried 20-30 cm below the ground. Since

https://doi.org/10.5194/essd-2026-99
Preprint. Discussion started: 10 April 2026

November 14, 2024, the underground part is heated by a self-regulating tube heating (QUINTEX GmbH, ILLW172CT/QX) to avoid condensation especially during summer. The flow rate is regulated at ~10 L min^{-1} (at 0 °C) by a needle valve and the tubing is protected by a filter (PTFE coated quartz fibre filter, 90 mm diameter, in a PFA filter holder) which is positioned ~38 m above the ground approximately 2 m from the sonic anemometer. The filter is replaced once every 2-6 weeks to prevent slight flow reductions due gradual buildup of aerosol on the filter. Mixing ratios of VOC's of > 500 individual masses < 1000 Th are measured and recorded at a 2Hz rate. Each hour, the air is diverted through a heated Pt-filter that burns all VOCs to CO_2 and H_2O during 10 minutes, hence reducing the concentrations to zero. This procedure serves as an effective zeroing method. In December 2024 a fast response dry chemiluminescence ozone analyser (Fast Ozone Sensor, Sextant Technologies) was installed. The instrument was installed in a heat insulated box in the tower at 35 m with a 5.5 m long 4 mm diameter Teflon tube to an inlet close to the sonic anemometer at 38.2 m height (Section 2.5). The flow is managed by an internal pump at a rate of 4.3 L min^{-1}. The instrument measures the intensity of light emitted during a chemiluminescent reaction between ozone in the reactor cell and a coumarin target with a highly sensitive photomultiplier. The instruments output is sampled at a rate of 20 Hz. The output voltage is directly proportional to the ozone concentration. However, the readings are sensitive to air pressure, temperature, humidity and flow rate and, over time, the coumarin target gradually becomes exhausted. Our experience is that the mV over ambient concentration signal decreases to about 25% of its original value after 2 to 3 weeks. Therefore, frequent calibrations are necessary. Initially, we did this by cross-calibrating the mean signal with the nearby national air quality monitoring network station 'Wekerom' (Air Quality Measuring Network, 2026), 6.6 km to the Southeast of the Loobos station. Although this makes the comparison somewhat dependant on wind direction, the coefficient of determination r^2 values are larger than 0.90 on a daily basis with hourly averaged concentrations. In March 2025 we installed a UV photometric Thermo 49C ozone analyser in the tower to improve the absolute concentration measurement and calibration procedure. The instrument is installed in the sea container at the bottom of the tower. Air is drawn in via the same inlet as the one towards the PTR-MS instrument and ozone concentrations are measured at a rate of 1 min^{-1}.

2.7.2 Flux calculation

The inlets of the tubes drawing air to the PTR-MS-ToF and Fast Ozone Sensor are located close to the sonic anemometer. This allows their signals to be correlated to the vertical velocity to quantify vertical fluxes. To validate the calculated fluxes, we perform two checks: 1) quantification and verification of the delay time caused by gas transport through the tubes 2) verification of the power spectra.

First, based on the tube diameter, length and flow rate, the expected travel time in the tubes is calculated (Table 9). The actual delay time may vary over time, because the flow rate may not be constant in time. The actual delay time may be estimated using the covariance optimisation method (Aubinet et al., 2012):

$$F = \overline{w'_t \, C'_{(t-t_{shift})}}$$

Where F is the vertical flux density, w' the vertical velocity deviation from the mean and C' the concentration deviation from the mean. t represents the measurement time and t_{shift} the delay time, which is determined by trying a range of delay times and selecting the one with the optimal F. For VOC's we smoothed the covariance as a function of delay time by applying a moving average of 11 timesteps of 0.5 s, because for some species the covariance function occasionally showed ill-defined peaks. In addition, the fluxes were calculated at a default delay time of 1 s for ozone and the delay time of monoterpenes for VOC's. Both w and C are subject to linear detrending. Because w is sampled at 20 Hz and VOC at 2 Hz, we subsampled the w signal to 2 Hz, respectively, when calculating VOC fluxes.

https://doi.org/10.5194/essd-2026-99
Preprint. Discussion started: 10 April 2026

Open Access Earth System Science Data Discussions

Table 9. Specifications of the tubes drawing air to the VOC and ozone sensors.

Gas	Tube inner diameter (mm)	Tube length (m)	Flow rate (L min^{-1})	Theoretical delay time (s)	Sample frequency (Hz)
VOC	6	56	10	8.6	2
Ozone	4	5.5	4.3	0.96	20

Figure 11 shows the resulting VOC and ozone fluxes as a function of the applied delay time for two selected times. The examples show that in general the detected delay time is close to the theoretical delay time. For each of the 4 VOC species, the detected delay times are between 6 and 8 seconds, which close to the theoretical 8.6 s value. In general, the automatic detection of the optimal delay time works best if the fluxes are large. The detection does not work as well for species and/or time period without a strong local source or sink, the procedure may fail. However, the delay time is not expected to change significantly over time. For ozone the automatic detection works well. Here the detected delay time (1.1 – 1.2 s) is again close to the theoretical one (0.96 s). We anticipate that for future definitive flux calculations, it would be best to apply an automatic time delay detection, while setting quite strict limits to the deviation from the most frequently detected and theoretical delay times. If the detected delay time is out of limits, the flux at a the most frequently detected delay time will be flagged.

In general, these results show that the VOC and ozone concentrations have sufficient quality to be used for flux calculation purposes.

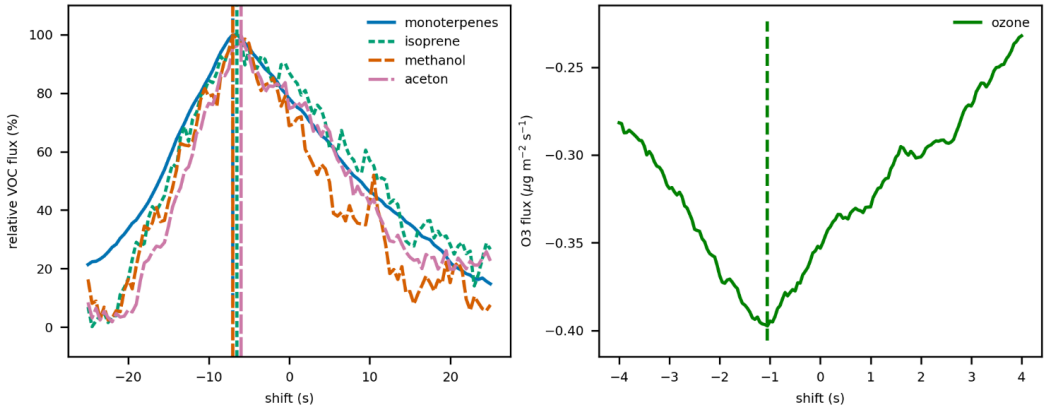

Figure 11. VOC (left, 8 July 2023 15:30 CET) and ozone (right, 7 December 2024, 11:30 CET) fluxes calculated for varying delay times between the vertical velocity and concentrations. The vertical dashed lines indicate the time when the maximum absolute flux occurs. The molar masses of the selected VOC's are monoterpenes: 137.132 Th , isoprene: 69.069 Th, methanol: 33.031 Th, acetone: 59.049 Th. For VOCs, the fluxes are normalised by dividing by the maximum absolute flux for that compound.

Second, an important question is if the VOC and ozone concentrations are collected at a sufficiently fast rate, close enough together and with small enough tube damping to not miss the high frequency part of the turbulence spectrum. As a first test, we calculate CO_2 fluxes, where we numerically reduce the sample rate from 20 Hz to 0.2 Hz. We do this by applying a block average to the CO_2 signal with block widths in a range between 1 and 1000 samples (averaging time $0.05 \leq \tau \leq 5$ s). Note that this represents a worst-case scenario, where we assume that a slower sampling frequency implies longer averaging times instead of less frequently collecting samples with a truly short sample collection time. The results show that applying block averages up to 2 s hardly change the calculated fluxes during this day and in most cases even an averaging time of 4 seconds still yields similar results as the original (Fig. Figure 12). This shows that, given the roughness of the forest and the high measurement location (38.2 m, 16 m above the canopy), the dominant eddies have a time scale longer than seconds and that

https://doi.org/10.5194/essd-2026-99
Preprint. Discussion started: 10 April 2026

the VOC and ozone sample collection frequencies of 2 and 20 Hz are fast enough for calculating turbulent fluxes. In subsequent analyses of spectra it may be relevant to remember that VOC's and ozone are reactive species, where the complexity of the reactions may affect the mixing lengths and shape of the spectra (Jonker et al., 2004).

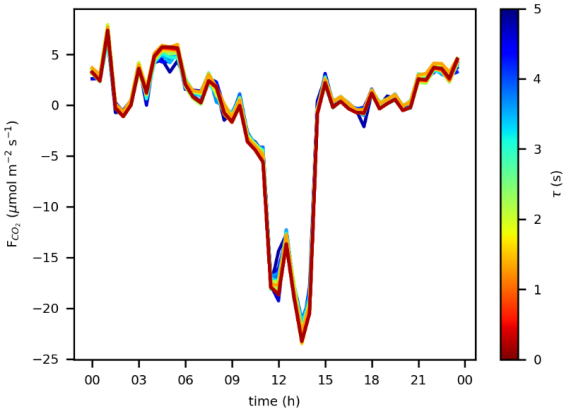

Figure 12. Diurnal time series of CO_2 fluxes calculated with a block average applied to the CO_2 signal with 26 block widths representing an averaging time τ between 0.05 and 5 s. The date is 28 June 2023.

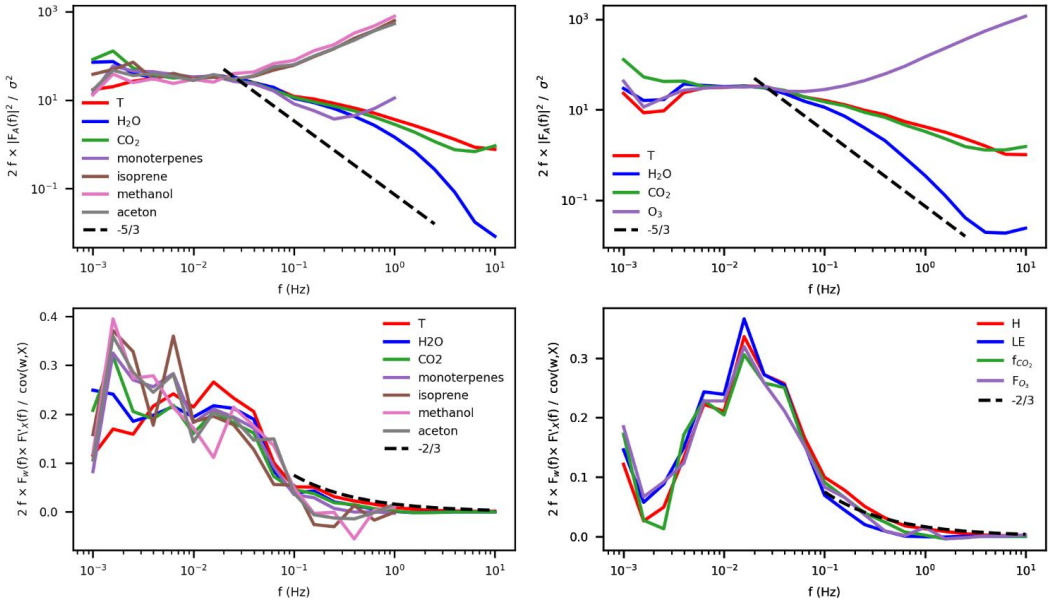

Figure 13. Spectra (top) and co-spectra (bottom) of VOCs on 7 July 2023 11:00-13:30h CET (left) and ozone on 17 May 2025 12:00-14:30h CET (right). All (Co)Spectra include temperature (T), water vapor and CO_2. The co-spectra are computed with a sample delay of 7.5 s and 1.2 s for VOC and O_3 fluxes, respectively. The dashed lines show the lines with -5/3 (top) and -2/3 (bottom) slopes, along which the spectra would be expected to develop in the inertial subrange.

We verify this statement by inspecting the power spectra and co-spectra of VOC and ozone concentrations and fluxes (Fig. Figure 13) in relation to those of temperature, water vapour and CO_2 measured by the EC system (Section 2.5). The shape of the power spectra are as expected (dashed line) for water vapour, while temperature and CO_2 concentration are subject to

https://doi.org/10.5194/essd-2026-99
Preprint. Discussion started: 10 April 2026

more variance at high frequencies than expected and ozone and particularly VOC concentrations show signs of high frequency noise, Nyquist folding and or low signal to noise ratio. The spectra have a better-defined shape when the fluxes are larger (e.g., T and CO_2 in July vs January). In principle, high frequency noise does not necessarily affect the calculated fluxes. Indeed, the co-spectra (bottom row in Fig. Figure 13) show that only waves up to a frequency of about 0.1-0.5 Hz contribute to co-variance. Higher frequency variations in concentrations are not correlated to vertical velocity. This corresponds to the results of our initial block averaging experiment (Fig. Figure 12), which showed that even averaging up to 2-5 s (0.5 – 0.2 Hz) does not significantly affect the calculated fluxes. Since our EC measurements are sampled at 20 and 2 Hz (Table 7), we are confident that we measure at sufficiently high rates for flux calculations. Nevertheless, the reason behind this high frequency noise should be studied in more detail. For isoprene, methanol and acetone the co-spectra are slightly negative between 0.1 and 1 Hz, the magnitude and shape of these fluxes appear to depend somewhat on the imposed delay time.

The analysis above verifies that the EC measurements of VOCs and ozone are of good quality and can be processed to fluxes. The concentration data will be processed to fluxes similar to the ICOS methodology (Sabatini et al., 2018, Dumont et al., 2026). Methods of calibrating the absolute concentration, non-linear sensitivity (Muller et al., 2010, Zahn et al., 2012, Dumont et al., 2026) and noise suppression (Aslan et al., 2020) will be described in more detail in future publications. The first version of the ozone concentration and flux data is available as van der Molen et al. (2026j).

2.8 Intermittent ecosystem characterisation

2.8.1 Digital Hemispheric Photography

To measure spatial and temporal variability in Green Area Index, digital hemispheric photographs (DHP) are taken. At the continuous measurement plots (CP's) photographs are taken every second month in a 9 point raster. At the 20 SP's photographs were taken once in a 5 point raster (Fig. S.2). The pictures are taken in conditions without direct sunlight, without rain or snow in the air or on the branches and leaves, not close to stems, branches or leaves. A Canon EOS 700D camera with a Sigma 4.5 lens with aperture F8, ISO 200 and shutter time < 1/30 s was used, which was installed level using a tripod. The photographs are stored in CR2 format, uploaded to ICOS and automatically processed. The procedure is explained in more detail in the ICOS Ecosystem Thematic Centre (ETC) 'Instructions for ancillary vegetation measurements in forest' (ICOS ETC, 2026). For the first year's results (Summer 2023 - Summer 2024), the LAI is estimated to vary between 2.2 and 2.8 m^2 m^{-2} , which is considerably larger than the earlier estimates (Figs. 5 and 6 in Zhao et al., 2025). To explain this difference, the earlier measurements will be repeated with the original instrument at the original locations and the DHP locations.

2.8.2 Leaf area and nutrient content

Each winter, needles are collected for foliar analysis. In each CP the 6 trees with the largest diameter are selected. From each of these trees, 2 or 3 twigs of the current year's cohort are collected, 30 in total. From 10 needles of each twig, the leaf area is measured with a flatbed scanner. Leaf mass is measured after oven drying the needles at 65 °C for 48 hours using a microscale.

From the same twigs, 20-30 g of needles are collected, dried at room temperature for 2-3 days and send to the ICOS Central Plant Analysis Laboratory, Villenave d'Ornon, France, for nutrient analysis, including N, C, P, K, Ca, Mg, Cu, Fe, Mn and Zn concentrations. Here we follow the ICOS ETC 'instructions for foliar samples collection and leaf mass to area ratio determination' (see ICOS ETC, 2026 for more details). The results of the 2024 campaign are listed in Table 10. The area, dry weight and C, N and P concentrations shown in Table 10 are in line with sampling campaigns performed in 1998, 1999, 2000, 2003 and 2012 (Table 7 in Zhao et al., 2025), although the variability between years is significant.

https://doi.org/10.5194/essd-2026-99
Preprint. Discussion started: 10 April 2026

555

Table 10. Mass, area and nutrient concentrations of foliar samples in 2024. In each Continuous Plots 15 foliar samples were collected from 10 trees (in total 30 samples). Each sample consists of 10 needles. The samples were dry weighed at 65 °C, the area measured, then submitted to the ICOS lab in France, where they were dried at 103 °C and analysed for nutrient concentrations.
560 **The samples were collected in March 2024/2025. The area and dry mass refer to the total over the 10 needles in a sample. The dry ratio is the ratio of mass at 103 °C and at 65 °C. The mean and standard deviation are calculated over the 15 samples per CP.**

	Plot	CP_01		CP_02	
		2024	2025	2024	2025
Area	cm^2	11.00 ± 2.31	11.30 ± 3.92	14.18 ± 3.81	7.78 ± 2.50
Dry weight	g	0.21 ± 0.06	0.29 ± 0.09	0.31 ± 0.13	0.27 ± 0.12
Dry ratio	%	91.11 ± 1.16	80.47 ± 4.42	91.53 ± 0.28	81.87 ± 5.18
Carbon	$gC\ kg^{-1}$	525.67 ± 2.85	528.33 ± 7.67	531.87 ± 3.50	527.13 ± 4.44
Nitrogen	$gN\ kg^{-1}$	17.35 ± 1.79	17.36 ± 1.97	18.24 ± 1.44	17.73 ± 1.22
Potassium	$gK\ kg^{-1}$	5.93 ± 1.14	5.41 ± 0.41	5.43 ± 0.61	5.40 ± 0.86
Calcium	$gCa\ kg^{-1}$	1.66 ± 0.28	2.48 ± 1.13	1.79 ± 0.66	2.05 ± 0.31
Phosporus	$gP\ kg^{-1}$	1.44 ± 0.22	1.32 ± 0.16	1.44 ± 0.12	1.40 ± 0.13
Manganese	$mgMn\ kg^{-1}$	172.40 ± 30.84	167.47 ± 31.96	139.95 ± 33.71	171.07 ± 30.00
Zinc	$mgZn\ kg^{-1}$	104.71 ± 42.37	127.61 ± 58.57	41.31 ± 11.19	110.26 ± 61.14
Iron	$mgFe\ kg^{-1}$	52.31 ± 6.17	51.57 ± 10.63	51.22 ± 8.17	52.29 ± 10.62
Copper	$mgCu\ kg^{-1}$	4.50 ± 0.65	4.33 ± 0.77	4.17 ± 0.55	4.55 ± 0.52
Magnesium	$gMg\ kg^{-1}$	0.89 ± 0.12	0.89 ± 0.26	0.83 ± 0.12	0.94 ± 0.21

2.8.3 Soil inventory

A soil inventory was carried out in Spring 2024 as part of the standard ICOS procedure. At each of the 20 SP's, 5 locations
565 were randomly assigned, 100 in total. At each location, first the organic layer was collected from a 25 × 25 cm area. Then an 8 cm diameter 100 cm deep soil core was taken. The core was divided into 5 sections: 0-5 cm, 5-15 cm, 15-30 cm, 30-60 cm and 60-100 cm. Photographs were taken from the core and/or a soil pit. The soil in each section was collected in a plastic bag. The samples were fresh weighed, dried, dry weighed, split into dead and life biomass (organic samples) and mineral soil and plant residue (mineral samples) to determine soil dry bulk density. The 600 samples have been sent to the ICOS ETC
570 European Soil Samples Conservatory in Orléans, France to be analysed for soil organic carbon and nitrogen content. A more detailed description of the procedure can be found in the ICOS ETC Instructions for soil sampling and preparation (ICOS ETC, 2026). The results of the 2024 campaign are not available yet. The soil inventory will be repeated with a 10-year interval.

2.9 Measurement campaigns and experiments

575 The renewed and extended infrastructure has been home to several intensive field campaigns and experiments. On 17 and 18 May 2022, an extensive campaign was held within the Ruisdael Observatory project (https://ruisdael-observatory.nl/, last access 4 February 2026). The aim was a characterization of the vertical and horizontal variability of meteorology and atmospheric constituents between grassland (Cabauw site) and the Loobos forest site. Besides the regular measurements, radio soundings were released to measure profiles of temperature, humidity and wind speed and direction. An aircraft (Sun et
580 al., 2023) was flown over the area several times per day to measure temperature, humidity, CO_2 concentration at a high

https://doi.org/10.5194/essd-2026-99
Preprint. Discussion started: 10 April 2026

frequency (50 Hz), which enabled the calculation of turbulent fluxes at different levels in the atmospheric boundary layer. Flasks were filled with air to be analysed for $\delta(O_2/N_2)$ ratio, CO, COS, CH_4, and the stable isotope concentrations $\delta^{13}C$ in CO_2 and $\delta^{18}O$ in H_2O. Manual measurements were performed at leaf level to measure photosynthesis rates and surface conductance. These data have been analysed for the relative contribution of surface and atmospheric signals, placing special emphasis on the individual contributions of processes that control the boundary layer development dynamics (Faasen et al., 2025).

The Loobos forest is immediately downwind from an area of major agricultural ammonia emissions. During two separate periods, an HT8700 open path ammonia analyser (Healthy Photon, inc.) was installed in combination with a miniDOAS to measure variations in NH_3 concentration and its absolute concentration. The experiment was held to test the setup, its applicability for eddy covariance flux calculations and if the setup could be installed operationally. The experiment and results are described in a paper by Melman et al. (2026).

A collaborative group consisting of researchers from Helmholtz Centre Potsdam, GFZ German Research Centre for Geosciences, TU Delft, Department of Geoscience and Remote Sensing, and University of Twente, ITC installed global navigation satellite system (GNSS) sensors at the top of the tower and at 5 locations underneath the canopy in an experiment to measure Vegetation Optical Depth (VOD). The data collection, analysis and verification is ongoing. GNSS data from GFZ systems is available upon request to Benjamin Brede (benjamin.brede@gfz.de). GNSS data from TU Delft will be published at https://gnss2.tudelft.nl/ and information and contact info can be found at http://m-wave.tudelft.nl/.

On 28 August 2024, a multi-scale experiment was performed using ground observations of Sun Induced Fluorences (SIF, ESA FloX), CO_2 fluxes and 10 Hz multiband incoming and outgoing radiation intensities installed at 8 different levels in the tower, an airborne Flying Laboratory of Imaging Systems (HyPlant and CzechGlobe), consisting of hyperspectral sensors CASI-1500, SASI-600 and TASI-600, and a LMS Q780 airborne full-waveform laser scanner. The measurement suite is complemented with TROPOMI satellite retrievals of SIF (Köhler et al., 2018). The purpose is to compare the retrieved data at different scales to work towards better understanding of ground, airborne and satellite observed data. Data inquiries via the corresponding authors.

A distributed temperature sensing (DTS) system is employed by the Civil Engineering & Geosciences, Water Resources group of Delft University of Technology (Schilperoort et al, 2024). Currently, the system aims at experimentally measuring dry and wet bulb temperatures along the tower in order to better understand transpiration and evaporation. Contact: Miriam Coenders (A.M.J.Coenders@tudelft.nl).

3 Demonstration of data

In this section, we demonstrate some of the capabilities of the station to measure the CO_2 fluxes. Section 3.1 shows how the total CO_2 flux is composed of a turbulent flux and a storage flux, and how the distribution over the two depends on the degree of turbulence. Section 3.2 shows how the CO_2 fluxes measured in the second tower (described in this paper) compare with the fluxes measured in the first tower (Zhao et al., 2025).

3.1 Distribution over turbulent and storage fluxes

The CO_2 flux measurements are composed of an eddy covariance part (section 2.5) and a storage fluxes part (section 2.5). Here we test if the combination of those systems is well-capable to measure the total flux. As mentioned, in sufficiently turbulent conditions, the entire flux is measured by the eddy covariance system, because the below canopy air is well-mixed with the surface layer, this is confirmed in Fig. Figure 14 below. In conditions with low turbulence intensity, such as may occur in calm, stable nights, the CO_2 respired from the ecosystem is hardly mixed to above canopy air and, it accumulates in the air below the canopy. We demonstrate this behaviour in Fig. Figure 14 for three nights in a row in September 2024, when

https://doi.org/10.5194/essd-2026-99
Preprint. Discussion started: 10 April 2026

the first night is very turbulent, the second night medium turbulent and the third night calm. The air temperatures are roughly similar each night, although the first night 1-2 °C colder than the other two.

In daytime conditions, the CO_2 gradient is typically less than 10 ppm from the top of the tower down to the forest floor. In the first night, the CO_2 profile is still relatively well mixed, $0.4 < u_* < 0.6$ m s^{-1} and the atmosphere only slightly stable with $(z-d)/L \approx 0.4$ (both u* and (z-d)/L are derived from the eddy covariance measurements at 38.2 m). The CO_2 gradient between the lowest (0.1 m) and second (0.4 m) is about 10 ppm and the gradient from 0.4 m to the top of the tower (38.2 m) is another 10 ppm. Hence, there is hardly any accumulation of CO_2 below the canopy. Hence the storage flux is close to 0 and the autotrophic and heterotrophic CO_2 respiration flux is properly measured by the eddy covariance system (about 5 µmol m^{-2} s^{-1}).

In the second night, turbulence intensity decreases, u_* decreases from 0.4 to 0.15 m s^{-1} and (z-d)/L increases from 0.1 to > 0.5. The turbulence is not sufficiently strong to mix all of the respired CO_2 to above the canopy. The CO_2 gradient is 120 ppm at the end of the night, with the average vertical 17 ppm per level between the surface and 11.2 m high, which, incidentally, shows that the height of the levels is well-chosen. Between 15.7 m and 38.2 m the total gradient is 5 ppm, which suggests that the gradient is built up from the soil surface upward. In this situation, the total flux is a mix of eddy covariance flux and storage flux, and the sum of both terms is roughly equal to the 5 µmol m^{-2} s^{-1} measured in the night before.

In the third night, the turbulence intensity is even smaller, $u_* < 0.1$ m s^{-1} until 6h in the morning, when it increases. The stability expressed by $(z-d)/L > 0.5$ in the evening and early night, afterwards it becomes unreliable under influence of small fluxes. The CO_2 strongly accumulates in the below canopy air, with the highest concentrations (730 ppm) near the ground, a total gradient of 230 ppm, which is distributed nearly even over the levels (~23 ppm $level^{-1}$), although the 15.7 m level exhibits concentrations closer to the 22.1 m level, suggesting respiration from the canopy crown contributes too CO_2 accumulation too. In this situation, the eddy covariance flux is indeed 0 and the total respiration – again roughly 5 µmol m^{-2} s^{-1} – is entirely represented by the storage flux. The onset of turbulence is at 6h in the morning, when the storage flux becomes negative (depletion of CO_2) and the eddy covariance flux becomes positive (upward flux). Later in the morning, photosynthesis becomes an important term. Interestingly, complete removal of the stored CO_2 below the canopy by photosynthesis takes until 9h in the morning, three hours after the onset of mixing at 6h. This figure also indicates that the below canopy air returns to well-mixed conditions at daytime again. Hence, ignoring the storage flux will not affect the daily total fluxes measured by the eddy covariance system, but it will affect its distribution over the day.

The above shows that the profile system is capable of measuring the buildup of vertical gradients below the eddy covariance system, thus complementing each other for the purpose of measuring the total CO_2 flux. However, horizontal advective fluxes may disturb the relation between the buildup of vertical gradients and the actual respiration flux. We did not measure advective fluxes, but it may be interesting to inspect the horizontal wind speeds above and below the canopy. In the first night, the windspeed at 38.2 m is 3.5 ± 1 m s^{-1}, 1.5 m s^{-1} at 22.1 m (canopy level), decreasing to below 1 m s^{-1}. Below the canopy, the windspeeds are 0.5 m s^{-1} or lower. In the second night, the 38.2 m windspeed decreases from 4 to 2 m s^{-1}, the 22.1 m windspeed decreases from 1 to 0.5 m s^{-1} and the below canopy windspeeds decrease from 0.5 to below 0.2 m s^{-1}. In the third night, the 38.2 m windspeed is intermittently between 0.5 and 1.0 m s^{-1} and between 1 and 2.5 m s^{-1}. The windspeeds at 22.1 and below are mostly in the order of 0.1 m s^{-1}, although the 22.1 m windspeed sometimes increases with the 38.2 m windspeed.

It appears that only in more calm and stable conditions, the windspeeds drop considerably below 1 m s^{-1}, in less calm nights the windspeed could be large enough to cause horizontal CO_2 advection. With a distance of 1.8 km to the nearest edge of the (spatially quite homogeneous) forest and a windspeed of 1 m s^{-1}, it would take 30 minutes for the wind to move from the forest edge to the station, during which horizontal gradients induced by the transition to forest may not be entirely settled.

https://doi.org/10.5194/essd-2026-99
Preprint. Discussion started: 10 April 2026

So, although there is no indication of an unbalance of the sum of turbulent and storage flux and the expected total flux of 5 µmol m^{-2} s^{-1}, we cannot guarantee that advective fluxes are absent at the site.

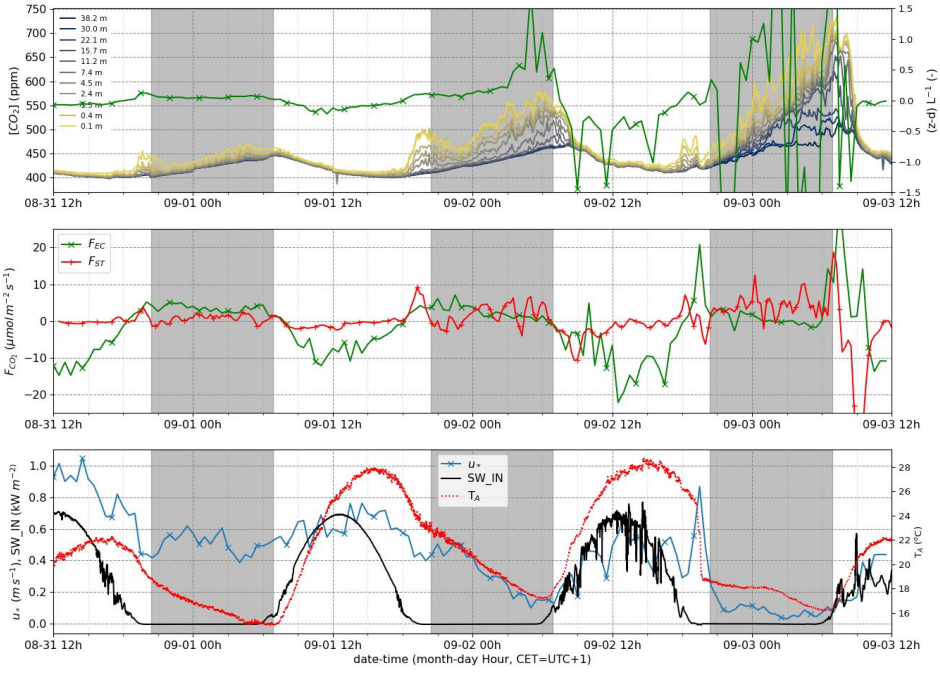

Figure 14. Top: CO_2 concentrations measured in the profile along the tower. Middle: Eddy covariance flux and storage flux. Bottom, left axis: u* and incoming shortwave radiation, right axis: air temperature at 2.4 m. These data were measured between 31 August and 3 September 2024. The shaded areas represent the time between sunset (20:24h CET) and sunrise (06:54h CET).

3.2 Continuity of NEE timeseries from the first tower to the second

The second tower (since 2021) is intended to continue the first tower measurements (1996-2023) and to build a continuous long-term timeseries. Since the measurement heights and instrumentation (open path and closed path gas analyser) were different, it is relevant to verify if the fluxes measured by the systems in the two towers match. Unfortunately, the gas analyser in the first tower suffered a breakdown for a long period after the second tower's eddy covariance system was installed. However, we do have a 2 month period of overlapping data in between 28 July and 29 September 2021. Fig Figure 15 shows the level to which the two datasets agree. The diurnal cycles show much agreement, even at nighttime, when below sensor storage could be different for the two systems. With a r^2 of 0.74 there is some random variability between the datasets, but the slope is close to 1 and the offset small relative to the magnitude of the fluxes. Here only data with quality flag 0 have been selected. Selecting data with quality flags 1 and/or 2 will result in a significantly worse match. Since the second tower was not yet labelled as an ICOS site, we use our own EddyPro results in this comparison. Fig. S.3, however, shows that there is a near 1:1 correspondence between our own EddyPro calculations and the ICOS ETC L2 and Near Real Time (NRT) results. These results combined suggest that the flux measurements of the first and second tower correspond to

https://doi.org/10.5194/essd-2026-99
Preprint. Discussion started: 10 April 2026

a high degree and there is no reason to expect differences between the CO_2 flux measurements. Thus we are confident that the second tower provides a true continuation of the first tower's CO_2 flux measurements.

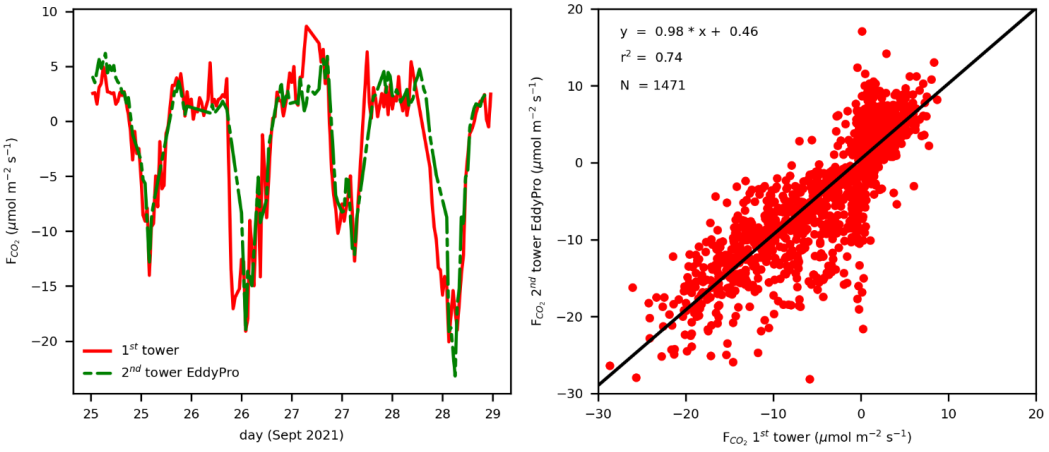

Figure 15. Comparison of the eddy covariance CO_2 fluxes measured by the first tower (Zhao et al., 2025) and the second tower. Left: the diurnal cycles over a subset of the two month period. Right: the correlation between the two datasets. Here only data with quality flag 0 have been selected.

4 Outlook: Positioning Loobos as a Leading Ecosystem Observatory in a Changing Climate

With the infrastructure and instruments outlined in this paper, we aim to establish Loobos as a flagship site within the international scientific community—a forefront ecosystem site for long-term, interdisciplinary ecosystem and atmospheric research. Our ambition is to contribute cutting-edge data and insights that inform both science and policy at national and global scales.

1. **Advancing Carbon Cycle Science**
   The installation of a second flux tower at Loobos marks a major step toward its labelling as an ICOS Class 2 Ecosystem Station. This enables us to extend the long-term carbon sequestration record initiated in 1996 (Zhao et al., 2025), capturing the forest's response to gradual, abrupt, and intermittent climate variability—including heatwaves, droughts, and pollution episodes. Our data will feed into the ICOS Carbon Portal, supporting a wide range of continental and global carbon budget assessments.
2. **Linking Air Quality and Ecosystem Functioning**
   By integrating measurements of VOCs, NOx, O_3, and NH_3, we investigate how fertilization, acidification and air pollution influence carbon uptake and forest health. Loobos is uniquely positioned downwind of one of the world's largest nitrogen-emitting regions, making it an ideal site to monitor the effects of evolving emission policies. Together with ICOS stations in Cabauw and Lutjewad, Loobos forms a strategic transect for studying sectoral emission impacts.
3. **Quantifying Forest Water Dynamics**
   We are measuring the forest's water consumption and yield to address growing concerns about hydrological imbalances in the Veluwe region—a critical source of drinking water. Our observations will provide a scientific foundation for advising policymakers on the role of forest type and management in sustainable water harvesting.
4. **Enabling Fundamental Ecosystem-Atmosphere Research**
   Loobos serves as a platform for advanced research into canopy-atmosphere exchange processes. We aim to deepen

https://doi.org/10.5194/essd-2026-99
Preprint. Discussion started: 10 April 2026

our understanding of radiation, heat, water, momentum, and trace gas fluxes—particularly the role of in-canopy gradients in shaping photosynthesis, stomatal behaviour, and deposition dynamics.

5. **Model Validation and Development**
   Our goal is to generate comprehensive datasets for validating next-generation multi-layer canopy models, including large-eddy simulations of turbulent exchange (Pedruzo-Bagozfgoitia et al., 2023) and the MLC-CHEM model (Ganzeveld et al., 2002; Visser et al., 2022).
6. **Coupling Canopy and Boundary Layer Meteorology**
   Understanding the interactions between canopy processes and boundary layer dynamics is essential for improving weather and climate models, especially those incorporating dynamic vegetation (Boussetta et al., 2013).
7. **Supporting Satellite and Aircraft Observations**
   Loobos plays a key role in satellite retrieval validation, in synergy with the Ruisdael/WUR research aircraft (PH-WUR), enhancing the accuracy of remote sensing products.
8. **Experimental DTS setup**
   The infrastructure is attractive to test experimental setups, such as the Distributed Temperature Sensing setup, installed by Delft University (Miriam Coenders and Gijs Vis)
9. **Hosting Targeted Field Campaigns**
   With its extensive infrastructure, Loobos is a prime location for field campaigns focused on boundary layer exchange and remote sensing calibration. Recent and ongoing campaigns include the canopy - boundary layer exchange experiment (Faassen et al., 2025), a 2024 HyPlant mission and GNSS studies by Delft, Twente, and Potsdam Universities.
10. **Fostering Interdisciplinary Collaboration**
    Loobos brings together expertise from carbon cycle science, hydrology, ecology, soil science, forestry, meteorology, and air quality. This interdisciplinary approach is vital for understanding ecosystem services—such as carbon storage, water regulation, and biodiversity—under increasing anthropogenic pressure and climate change.

5 Data availability

All data described in sections 2.2-2.4 and 2.6-2.7 are uploaded to https://MAQ-Observations.nl (last access 4 February 2026) every 30 minutes and to the ICOS Carbon Portal (2026) on a daily basis. Our data is available in near real-time, including customizable charts, at MAQ-Observations. The data are available for use according to a CC-BY 4.0 data licence. Any used data must be cited accordingly, please refer to https://maq-observations.nl/maq-data-license/ (last access 4 February 2026) and https://www.icos-cp.eu/how-to-cite (last access 4 February 2026). On the ICOS Carbon Portal we recommend to look for the L2 product for previous years and to the Near-Real-Time (NRT) data product for the ongoing year. The PhenoCam data are accessible via https://phenocam.nau.edu/webcam/sites/nlloobs/ (last access 4 February 2026). All data described in other sections are available for use according to the same licenses too, please contact the authors of this paper to obtain access.

ICOS Level 2 (L2) products are available via:

- ETC L2 **Archive** from Loobos 2023-01-01–2025-10-01: https://doi.org/11676/RBbGtSvPuyjgktNpRDUq5fpw (van der Molen et al., 2026a)
- ETC L2 **Meteosens** from Loobos 2022-12-31–2025-09-30: https://doi.org/11676/ue7IUwhI1eSbNEsFZtbvWjur (van der Molen et al., 2026b)
- ETC L2 **Meteo** from Loobos 2022-12-31–2025-09-30: https://doi.org/11676/7OvfpkiXvumy_vSHQ6ds3Zbo (van der Molen et al., 2026c)

https://doi.org/10.5194/essd-2026-99
Preprint. Discussion started: 10 April 2026

- ETC L2 **Fluxes** from Loobos 2022-12-31–2025-09-30: https://doi.org/11676/Ww4zYPNKHkBUcjZxNS4CXN1j (van der Molen et al., 2026d)
- ETC L2 **Auxdata** from Loobos 2023-05-10–2025-10-01: https://doi.org/11676/N3zBxhFvmOdlkXIW8jwryl-A (van der Molen et al., 2026e)

ICOS Near Realtime Observational Data (NRT, Level 1) are available via:

- ETC NRT **Meteosens** from Loobos, 2025-09-30–2026-02-02: https://doi.org/11676/dsr4zZ3uWWcwSAHl5VnaPK2V (van der Molen et al., 2026f)
- ETC NRT **Meteo** from Loobos, 2025-09-30–2026-02-02: https://doi.org/11676/ZYwePVBwSnQfO8buNlkj3r8f (van der Molen et al., 2026g)
- ETC NRT **Fluxes** from Loobos, 2025-09-30–2026-02-02: https://doi.org/11676/-l_yUYF4afS0hfT__FLxpmNJ (van der Molen et al., 2026h)
- ETC NRT **AuxData** from Loobos, 2025-09-30–2026-02-02: https://doi.org/11676/fnL4vgIPrGLXLD-O97gpZ9cB (van der Molen et al.,2026i).

- ICOS Forest ancillary data are available via: https://icos.uantwerpen.be/Content/AncillaryReports/NL-Loo_Ancillary_Report.html (Iserbyt et al., 2026) (will be merged with ICOS-cp.eu)
- The Ozone concentration and flux data will be published as annual archives. The 2025 data are available via https://doi.org/10.17887/WUR01-6UGU9F (van der Molen et al., 2026j). Intermediate data are available upon request.

6 Code availability

The Python codes for processing the data and plotting figures 9, 11 – 15 and S.3 can be found at https://git.wur.nl/molen050/loobos-second-tower-reference-paper.

Acknowledgements

The second Loobos tower and its instrumentation is funded by the Dutch Science Fund (NWO, 2026) via the Ruisdael Observatory (2026) grant. The station is built on land owned by the Dutch National Forest Service (Staatsbosbeheer). We acknowledge payment of the ICOS station fees by the Ministry of Infrastructure and Water Management.

The PhenoCam was kindly supplied by Yunpeng Luo (Ecosystems Ecology, Forest Dynamics group, Swiss Federal Institute for Forest, Snow and Landscape Research WSL) as part of the Velux project (https://veluxstiftung.ch/). Data used in this research were provided by the PhenoCam Network, which has been supported by the National Science Foundation, the Long-Term Agroecosystem Research (LTAR) network which is supported by the United States Department of Agriculture (USDA), the U.S. Department of Energy, the U.S. Geological Survey, the Northeastern States Research Cooperative, and the USA National Phenology Network. We thank the PhenoCam Network collaborators, including station PIs and technicians, for publicly sharing the data that were used in this paper.

We acknowledge the support of staff and students from Wageningen University during the tree and soil inventory field campaigns and lab analysis.

We thank Roel Dijksma (Hydrology and Environmental Hydraulics, Wageningen University) for explaining the geological history and verifying the description.

We used Microsoft Copilot to help better structure parts of the manuscript.

https://doi.org/10.5194/essd-2026-99
Preprint. Discussion started: 10 April 2026

Author contribution

MvdM is the station PI. He conceptualized the study and wrote the manuscript. HS is the station technician, he conducted sampling, collected the manual data and maintained the site. RH, JF and LG is responsible for the VOC, ozone and NO_2 measurements, JB and HZ are responsible for data storage, data processing and data verification. WP, MK, JV, LG and BK have been and are responsible for continuity of the station in terms of finances, proposal writing and scientific output. All authors reviewed and revised the manuscript.

Competing interests

The contact author declares that none of the authors have any competing interests.

References

Air Quality Measuring Network, 2026: https://www.luchtmeetnet.nl/meetpunten?station=NL10738&component=O3, last access: 4 February 2026.

Aubinet, M., Vesala, T., and Papale, D. (Eds.): Eddy Covariance, Springer Netherlands, Dordrecht, https://doi.org/10.1007/978-94-007-2351-1, 2012.

Aslan, T., Peltola, O., Ibrom, A., Nemitz, E., Rannik, Ü., and Mammarella, I.: The high-frequency response correction of eddy covariance fluxes – Part 2: An experimental approach for analysing noisy measurements of small fluxes, Atmos. Meas. Tech., 14, 5089–5106, https://doi.org/10.5194/amt-14-5089-2021, 2021.

Bakker, M. A. J. and van der Meer, J. J. M.: Structure of a Pleistocene push moraine revealed by GPR: the eastern Veluwe Ridge, The Netherlands. Geological Society London Special Publications, 211(1):143-151, https://doi.org/10.1144/GSL.SP.2001.211.01.12, 2023

Benneth, M. R.: The morphology, structural evolution and significance of push moraines. Earth Sci. Rev., 53(3), 197-236. https://doi.org/10.1016/S0012-8252(00)00039-8, 2001.

Berg, M.W. and Beets, D. J.: Saalian glacial deposits and morphology in the Netherlands. In: J.J.M. van der Meer (ed) Tills and Glaciotectonics. Balkema, Rotterdam, 223-251, 1987.

Boussetta, S., et al., Natural land carbon dioxide exchanges in the ECMWF integrated forecasting system: Implementation and offline validation, J. Geophys. Res. Atmos., 118, 5923–5946, doi:10.1002/jgrd.50488, 2013.

CLO, 2026: CBS Statistics Netherlands, The Hague; PBL Netherlands Environmental Assessment Agency, The Hague; RIVM National Institute for Public Health and the Environment, Bilthoven; and Wageningen University and Research, Wageningen. Stikstofdepositie, (EN: Nitrogen deposition, 1990-2024) (indicator 0189, version 22, 9 October 2025), https://www.clo.nl/indicatoren/nl018922-stikstofdepositie-1990-2024 , last access 4 February 2026.

Data and Information on the Dutch Subsurface, 2026: https://www.dinoloket.nl/en/subsurface-models/map, select BRO REGIS II v2.2.2 and draw a cross section (NL: doorsnede) using the menu on the right, last access: 6 February 2026.

Dolman, A. J., Moors, E. J., Elbers, J. A., and Snijders, W.: Evaporation and surface conductance of three temperate forests in the Netherlands, Ann. For. Sci., 55, 255-270, https://doi.org/10.1051/forest:19980115, 1998.

Dumont, C., Verreyken, B. W. D., Schoon, N., Bergmans, B., Heinesch, B., and Amelynck, C.: Multi-year observations of BVOCs and ozone: concentrations and fluxes measured above and below the canopy in a mixed temperate forest, Earth Syst. Sci. Data, 18, 617–654, https://doi.org/10.5194/essd-18-617-2026, 2026.

https://doi.org/10.5194/essd-2026-99
Preprint. Discussion started: 10 April 2026

Dutch Mycological Association, 2017: Parasitaire schimmel op Amerikaanse vogelkers verovert Nederland (EN: Parasitic fungus on Prunus Serotina conquers the Netherlands, Nature Today, https://www.naturetoday.com/intl/nl/nature-reports/message/?msg=23523, last access: 4 February 2026.

de Vries, W. and E. Du: Chapter 1 - Nitrogen deposition and its impacts on forest ecosystems: A global perspective, In: Editor(s): Atmospheric Nitrogen Deposition to Global Forests Enzai, Du, Wim de Vries (Eds), 1-13, Academic Press, https://doi.org/10.1016/B978-0-323-91140-5.00013-0, 2024.

Faassen, K., González Armas, R., Koren, G., Adnew, G. A., van Asperen, H., Botía, S., Hartogensis, O., Hutjes, R., Miller, J., van der Molen, M., Luijkx, I. T., & Vilà-Guerau de Arellano, J.: Tracing diurnal variations of atmospheric CO_2, O_2 and $\delta^{13}CO_2$ over a tropical and a temperate forest. Geophys. Res. Letters, 52 (20), https://doi.org/10.1029/2025GL118016, 2025.

FLUXNET, 2010: https://fluxnet.org/data/la-thuile-dataset/lathuile-data-summary/, last access: 25 February 2026.

Fratini, G., Sabbatini, S., Ediger, K., Riensche, B., Burba, G., Nicolini, G., Vitale, D., and Papale, D.: Eddy covariance flux errors due to random and systematic timing errors during data acquisition, Biogeosciences, 15, 5473–5487, https://doi.org/10.5194/bg-15-5473-2018, 2018.

Ganzeveld, L.N., Lelieveld, J., Dentener, F.J., Krol, M.C. and Roelofs, G.J.. Atmosphere-biosphere trace gas exchanges simulated with a single-column model. J. Geophys. Res. Atmos., 107(D16): ACH-8. https://doi.org/10.1029/2001JD000684, 2002.

Geiger, R.: "Klassifikation der Klimate nach W. Köppen" [Classification of climates after W. Köppen]. Landolt-Börnstein – Zahlenwerte und Funktionen aus Physik, Chemie, Astronomie, Geophysik und Technik, alte Serie. Vol. 3. Berlin: Springer. pp. 603–607, 1954.

Jonker, H.J.J., Vilà-Guerau de Arellano, J. and Duynkerke, P. G.: Characteristic Length Scales of Reactive Species in a Convective Boundary Layer. *J. Atmos. Sci.*, 61, 41–56, https://doi.org/10.1175/1520-0469(2004)061<0041:CLSORS>2.0.CO;2, 2004

ICOS Carbon Portal, 2026: https://www.icos-cp.eu, last access: 4 February 2026.

ICOS ETC, 2026: https://www.icos-etc.eu/icos/documents/instructions, last access: 4 February 2026.

Iserbyt, A., Trotta, C., Op de Beeck, M. and Bert Gielen, Summary Ancillary Data for NL-Loo, 2026, https://icos.uantwerpen.be/Content/AncillaryReports/NL-L6o_Ancillary_Report.html (last access: 4 February 2026)

Kljun, N., Calanca, P., Rotach, M. W., and Schmid, H. P.: A simple two-dimensional parameterisation for Flux Footprint Prediction (FFP), Geosci. Model Dev., 8, 3695–3713, https://doi.org/10.5194/gmd-8-3695-2015, 2015.

Köehler, P., Frankenberg, C., Magney, T. S., Guanter, L., Joiner, J., & Landgraf, J.: Global retrievals of solar-induced chlorophyll fluorescence with TROPOMI: First results and intersensor comparison to OCO-2. Geophys. Res. Lett., 45, 10,456–10,463. https://doi.org/10.1029/2018GL079031, 2018.

MAQ Observations (2026): https://MAQ-Observations.nl, last access: 4 February 2026.

Melman, E.A., Rutledge-Jonker, S., Frumau, K.F.A., Hensen, A., van Pul, W.A.J., Stolk, A.P., Wichink Kruit, R.J., van Zanten, M.C.: Measurements and model results of a two-year dataset of ammonia exchange over a coniferous forest in the Netherlands, Atmos. Environ., 344, https://doi.org/10.1016/j.atmosenv.2024.120976, 2025.

Melman, E.A., Wintjen, P., de Boer, J., Eijkelboom, M., Felter, K., Haaima, M., Hensen, A., van der Hoff, R., van Mansom, H., van der Molen, M.K., Voorneveld, M., Rutledge-Jonker, S., Snellen, H., Vila-Guerau de Arellano, J., Wichink Kruit,

https://doi.org/10.5194/essd-2026-99
Preprint. Discussion started: 10 April 2026

R.J., Zhang, J., and van Zanten, M.C.: Biosphere-Atmosphere Ammonia Exchange from a Forest Ecosystem Perspective. Submitted to Agricultural and Forest Meteorology, 2026.

Muller, J. B. A., Percival, C. J., Gallagher, M. W., Fowler, D., Coyle, M., and Nemitz, E.: Sources of uncertainty in eddy covariance ozone flux measurements made by dry chemiluminescence fast response analysers, Atmos. Meas. Tech., 3, 163–176, https://doi.org/10.5194/amt-3-163-2010, 2010.

NWO, 2026: https://www.nwo.nl, last access: 4 February 2026.

Pastorello, G., Trotta, C., Canfora, E. et al.: The FLUXNET2015 dataset and the ONEFlux processing pipeline for eddy covariance data. Sci. Data, **7**, 225, https://doi.org/10.1038/s41597-020-0534-3, 2020.

Pedruzo-Bagazgoitia, X., Patton, E.G., Moene, A. F., Ouwersloot, H. G.,Gerken, T., Machado, L. A. T., et al. Investigating the diurnal radiative,turbulent, and biophysical processesin the Amazonian canopy-atmosphereinterface by combining LES simulationsand observations. J. Adv. Model. Earth Syst.,15, e2022MS003210. https://doi.org/10.1029/2022MS003210, 2023.

PhenoCam, 2026: https://phenocam.nau.edu/webcam/sites/nlloobs/, last access: 4 February 2026.

Richardson, A. D., Hufkens, K., Milliman, T., Aubrecht, D. M., Chen, M., Gray, J. M., Johnston, M. R., Keenan, T. F., Klosterman, S. T., Kosmala, M., Melaas, E. K., Friedl, M. A., and Frolking, S.:Tracking vegetation phenology across diverse North American biomes using PhenoCam imagery. Sci. Data, 5, Article number: 180028, https://doi.org/10.1038/sdata.2018.28, 2018.

Ruegg, G. H. J.: Glaciofluvial and glaciolacustrine deposits in the Netherlands. In: Ehlers, J. (ed) Glacial Deposits in North-West Europe. Balkema, Rotterdam, 279-392, 1983.

Ruisdael Observatory, 2026: https://Ruisdael-Observatory.nl, last access: 4 February 2026.

Sabbatini, S., Mammarella, I., Arriga, N., Fratini, G., Graf, A., Hörtnagl, L., Ibrom, A., Longdoz, B., Mauder, M., Merbold, L., Metzger, S., Montagnani, L., Pitacco, A., Rebmann, C., Sedlák, P., Šigut, L., Vitale, D., and Papale, D.: Eddy covariance raw data processing for CO_2 and energy fluxes calculation at ICOS ecosystem stations. Int. Agrophys., 32(4), pp.495-515, https://doi.org/10.1515/intag-2017-0043, 2018.

Schelhaas, M. J., Teeuwen, S., Oldenburger, J., Beerkens, G., Velema, G., Kremers, J., Lerink, B., Paulo, M. J., Schoonderwoerd, H., Daamen, W., Dolstra, F., Lusink, M., van Tongeren, K., Scholten, T., Pruijsten, I., Voncken, F., Clerkx, A. P. P. M.: Zevende Nederlandse Bosinventarisatie: Methoden en resultaten (Seventh Dutch Forest Inventory: Methods and results). WOt-report; No. 142, 127 pp. WOT Natuur & Milieu. https://doi.org/10.18174/571720, 2022.

Schilperoort, B., Jiménez Rodríguez, C., van de Wiel, B., & Coenders-Gerrits, M.: A distributed-temperature-sensing-based soil temperature profiler. Geoscientific Instrumentation, Methods and Data Systems, 13(1), 85-95. https://doi.org/10.5194/gi-13-85-2024, 2024.

Seyednasrollah, B., Young, A. M., Hufkens, K., Milliman, T., Friedl, M. A., Frolking, S., and Richardson, A. D.: Tracking vegetation phenology across diverse biomes using version 2.0 of the phenocam dataset. Sci. Data, 6(1):222, https://doi.org/10.1038/s41597-019-0229-9, 2019.

Spek, T., and Kleine Koerkamp, K.: Middeleeuwse ijzer- en houtskoolproductie op de Veluwe. Nieuw onderzoek van een productielandschap in het bosgebied 't Asselt bij Rheden (Veluwezoom). (Medieval iron and charcoal production on the Veluwe. New research of a production landscape in the forest area 't Asselt near Rheden (Veluwezoom). Tijdschrift voor Historische Geografie (Journal for Historical Geography) 7(1), 3-25. In Dutch with English Abstract. https://doi.org/10.5117/THG2022.1.001.SPEK, 2022.

https://doi.org/10.5194/essd-2026-99
Preprint. Discussion started: 10 April 2026

Sun, Y., Jia, L., Chen, Q., Lin, X., Sude, B., Quan, Z., Hutjes, R. W. A: Construction of a spatially gridded heat flux map based on airborne flux Measurements using remote sensing and machine learning methods, Agric. For. Meteorol., 334, https://doi.org/10.1016/j.agrformet.2023.109424, 2023.

Topo Time Travel, Kadaster, 2026: https://topotijdreis.nl/kaart/1911/@179163,464208,8.71, last access: 4 February 2026.

van der Molen, M., Barten, S., Kruijt, B., Lootens, R., Snellen, H., Zhao, H., ETC L2 **Archive** from Loobos 2023-01-01–2025-10-01, ICOS RI, https://doi.org/11676/RBbGtSvPuyjgktNpRDUq5fpw, 2026a

van der Molen, M., Barten, S., Kruijt, B., Lootens, R., Snellen, H., Zhao, H., ETC L2 **Meteosens** from Loobos 2022-12-31–2025-09-30, ICOS RI, https://doi.org/11676/ue7IUwhI1eSbNEsFZtbvWjur, 2026b

van der Molen, M., Barten, S., Kruijt, B., Lootens, R., Snellen, H., Zhao, H., ETC L2 **Meteo** from Loobos 2022-12-31–2025-09-30, ICOS RI, https://doi.org/11676/7OvfpkiXvumy_vSHQ6ds3Zbo, 2026c

van der Molen, M., Barten, S., Kruijt, B., Lootens, R., Snellen, H., Zhao, H., ETC L2 **Fluxes** from Loobos 2022-12-31–2025-09-30, ICOS RI, https://doi.org/11676/Ww4zYPNKHkBUcjZxNS4CXN1j, 2026d

van der Molen, M., Barten, S., Kruijt, B., Lootens, R., Snellen, H., Zhao, H., ETC L2 **Auxdata** from Loobos 2023-05-10–2025-10-10, ICOS RI, https://doi.org/11676/N3zBxhFvmOdlkXIW8jwryl-A, 2026e

van der Molen, M., Barten, S., Kruijt, B., Lootens, R., Snellen, H., Zhao, H., ETC NRT **Meteosens** from Loobos, 2025-09-30–2026-02-02, ICOS RI, https://doi.org/11676/dsr4zZ3uWWcwSAHI5VnaPK2V, 2026f

van der Molen, M., Barten, S., Kruijt, B., Lootens, R., Snellen, H., Zhao, H., ETC NRT **Meteo** from Loobos, 2025-09-30–2026-02-02, ICOS RI, https://doi.org/11676/ZYwePVBwSnQfO8buNlkj3r8f, 2026g

van der Molen, M., Barten, S., Kruijt, B., Lootens, R., Snellen, H., Zhao, H., ETC NRT **Fluxes** from Loobos, 2025-09-30–2026-02-02, ICOS RI, https://doi.org/11676/-l_yUYF4afS0hfT__FLxpmNJ, 2026h

van der Molen, M., Barten, S., Kruijt, B., Lootens, R., Snellen, H., Zhao, H., ETC NRT **AuxData** from Loobos, 2025-09-30–2026-02-02, ICOS RI, https://doi.org/11676/fnL4vgIPrGLXLD-O97gpZ9cB, 2026i

van der Molen, M.K., Barten, J.G.M. and Ganzeveld, L.: NL-Loo_O3_2025: Ozone concentration and flux observations at Loobos, NL – 2025, https://doi.org/10.17887/WUR01-6UGU9F, 2026j.

van der Wateren, F. M.:. Structural geology and sedimentology of push moraines: processes of soft sediment deformation in a glacial environment and the distribution of glaciotectonic styles. Mededelingen Rijks Geologische Dienst (Memo's of the National Geological Service), 54, 1-168, http://dx.doi.org/10.1016/S0277-3791(98)00120-6, 1995.

Visser, A.J., Ganzeveld, L.N., Finco, A., Krol, M.C., Marzuoli, R. and Boersma, K.F.. The combined impact of canopy stability and soil NOx exchange on ozone removal in a temperate deciduous forest. J. Geophys. Res. G: Biogeosciences, 127(10): e2022JG006997. 2022.

Witte, C.: Stuifzandbestrijding op de Veluwe 1500-1884. De invloed van gewestelijk overheidsbeleid op het functioneren van de buurschap Harskamp als collectieve institutie (Drift sand control on the Veluwe 1500-1884. The influence of regional government policy on the functioning of the Harskamp neighbourhood as a collective institution). MSc Thesis Groningen University, https://www.rug.nl/research/kenniscentrum-landschap/voor-studenten/masterscripties/masterscripties. 2016.

Zahn, A., Weppner, J., Widmann, H., Schlote-Holubek, K., Burger, B., Kühner, T., and Franke, H.: A fast and precise chemiluminescence ozone detector for eddy flux and airborne application, Atmos. Meas. Tech., 5, 363–375, https://doi.org/10.5194/amt-5-363-2012, 2012.

https://doi.org/10.5194/essd-2026-99
Preprint. Discussion started: 10 April 2026

Zhao, H., Dolman, H., Elbers, J., Jans, W., Kruijt, B., Moors, E., Snellen, H., Vila-Guerau de Arellano, J., Peters, W., Krol, M., Hutjes, R., and van der Molen, M.: The Loobos ecosystem first tower dataset: meteorology, turbulent fluxes and net ecosystem exchange (1996 to 2021), Earth Syst. Sci. Data Discuss. [preprint], https://doi.org/10.5194/essd-2025-372, in review, 2025.